Department of Physics and Astronomy

Heidelberg University

Master thesis

in Physics

submitted by

Lara Sophie Grabitz

born in Essen

2022

ALP across the scales – Searches for axion-like particles in high energy and flavor observables

This Master thesis has been carried out by Lara Sophie Grabitz

at the

Institute for Theoretical Physics Heidelberg

under the supervision of

Jun.-Prof. Dr. Susanne Westhoff

ALPs quer über die Skalen – Suche nach axionähnlichen Teilchen in Hochenergie- und Flavor-Observablen:

Das axionähnliche Teilchen (ALP) ist ein pseudoskalares Teilchen jenseits des Standardmodells. Es ein gut motivierter Kandidat für dunkle Materie, ein möglicher Vermittler zu Teilchen dunkler Materie und löst in Spezialfällen auch das starke CP-Problem. Die ALP-Kopplungen an Teilchen des Standardmodells sind renormiert und laufen daher zwischen den Skalen. Sie können sowohl mit Hochenergie- als auch mit Flavor-Observablen gut eingeschränkt werden. Durch die Implementierung der Renormierungsgruppengleichungen können wir Observablen aus verschiedenen Energieskalen kombinieren. Wir haben die $t\bar{t}$-Produktion, die $t\bar{t}t\bar{t}$-Produktion und die Dijet-Winkelverteilung analysiert und dadurch Einschränkungen für die Kopplungen an Fermionen $C_{ff}(\Lambda)$ und Gluonen $C_{GG}(\Lambda)$ erhalten. Die Suchen nach $B \to KX(\to l^+l^-)$ und $B \to K\not{E}$ haben eine starke Sensitivität für die ALP-Fermionen-Kopplung $C_{ff}(\Lambda)$ und eine viel schwächere, aber nicht zu vernachlässigende Sensitivität für die ALP-W-Bosonen-Kopplung $C_{WW}(\Lambda)$. Das Zusammenspiel der Kopplungen in den Renormierungsgruppengleichungen begrenzt die Aussagekraft von Analysen für einzelne Kopplungen und unterstreicht die Notwendigkeit eines globalen Fit. Diese Arbeit geht einen ersten Schritt in diese Richtung.

ALPs across the scales – Searches for axion-like particles in high energy and flavor observables:

The axion-like particle (ALP) is a pseudoscalar particle beyond the Standard Model. It is a well motivated candidate for dark matter, a possible mediator to the dark sector and in some special cases might even solve the strong CP problem. ALP couplings to Standard Model particles run across the scales and are therefore renormalized. They can be well constrained with both high energy and flavor observables. By the implementation of the renormalization group equations we can combine observables from different energy scales. We analysed $t\bar{t}$ production, the $t\bar{t}t\bar{t}$ production and dijet angular distribution, yielding constraints on the couplings to fermions $C_{ff}(\Lambda)$ and gluons $C_{GG}(\Lambda)$. The searches for $B \to KX(\to l^+l^-)$ and $B \to K\not{E}$ have a strong sensitivity to the ALP-fermion coupling $C_{ff}(\Lambda)$ and a much weaker but nevertheless significant sensitivity to the ALP-W boson coupling $C_{WW}(\Lambda)$. The interplay of the couplings in the renormalization group equations limits the meaningfulness of fits for a single coupling and highlight the need for a global fit for which this work provides a first step.

Contents

1 Introduction

It is well known that the tremendously successful Standard Model (SM) has many shortcomings. [1] A possible solution to the strong CP problem is the axion, which is the pseudo-Nambu-Goldstone boson of a newly introduced Peccei-Quinn symmetry. [2–5] The presence of an axion-like particle (ALP) can also bring light into the search for dark matter: It is a candidate for dark matter [6, 7] as well as a possible mediator between dark and regular matter [8, 9].

After previous unsuccessful searches for heavier particles beyond the Standard Model, there is also increased research interest in the search for light, weakly coupling particles, such as the (pseudo)scalar ALP, in addition to the search for particles of ever higher masses. [10]

The ALP couplings to the Standard Model particles are running across the scales. Different observables at different scales therefore provide different constraints on the ALP couplings. Our implementation of the renormalization group equations gives us a powerful framework to combine the different constraints from high energy and flavor observables in one fit. Thus our constraints on the ALP couplings to fermions, gluons and W bosons are a first step towards a global fit.

This thesis is structured as following: We first give an introduction into ALPs and the underlying Lagrangian and explain the running across the scales. Section 3 explains the treatment of statistics and our implementation of the renormalization group equations. In Section 4 we investigate the phenomenology of ALPs: The $t\bar{t}$ production and the $t\bar{t}t\bar{t}$ production analyses constrain the ALP couplings to gluons $C_{GG}(\Lambda)$ and to fermions $C_{ff}(\Lambda)$. The dijet angular distribution analysis constrains the ALP-gluon coupling $C_{GG}(\Lambda)$. The analysis of searches in B meson decays for displaced particles $B \to KX(\to l^+l^-)$ and for missing energy $B \to K\not{E}$ constrain the ALP coupling to fermions and B mesons. In Section 5 we combine our analyses to a fit and give an outlook to open questions and future work.

The research in this thesis has been carried out in close collaboration with Sebastian Bruggisser.

2 Axion-like particles

This Section presents and describes the ALP Lagrangian and how the couplings derive from it. Then an alternative Lagrangian with the redundant Higgs operator is explored. The ALP evolution across the scales is described in the last part of this section.

2.1 The effective ALP Lagrangian

The axion-like particle (ALP) is the pseudo-Nambu-Goldstone boson of a spontaneously broken global $\mathrm{U}(1)_i$ symmetry and is a pseudoscalar Standard Model singlet. The ALP mass is protected by the shift symmetry $a \to a + c$ which arises from the $\mathrm{U}(1)$ symmetry. The small mass term softly breaks the continuous symmetry into a discrete symmetry. Quantum corrections can only break this symmetry to a certain degree which ensures that the mass stays light and protects the ALP from a fine-tuning problem. Because of this shift symmetry, the ALP field can only occur as a derivative in the Lagrangian. This results in a term of mass dimension 5 so that the couplings are suppressed by the ALP decay constant f. It is defined by the ALP cutoff scale Λ, which denotes the scale of new physics, with the relation:

$$\Lambda = 4\pi f \tag{2.1}$$

Higher order terms are suppressed by $(E/f)^2$, with the typical energy E, and can be neglected. The general effective Lagrangian up to dimension-5 is given by: [11]

$$\begin{aligned}\mathcal{L}_{\text{eff}}^{D\leq 5} = \frac{1}{2}\left(\partial_\mu a\right)\left(\partial^\mu a\right) - \frac{m_{a,0}^2}{2}\, a^2 \\ + \frac{\partial^\mu a}{f} \sum_F \overline{\psi}_F\, \boldsymbol{C}_F\, \gamma_\mu\, \psi_F + C_{GG}\,\frac{\alpha_s}{4\pi}\,\frac{a}{f}\, G^a_{\mu\nu}\,\tilde{G}^{a,\mu\nu} \\ + C_{WW}\,\frac{\alpha_2}{4\pi}\,\frac{a}{f}\, W^A_{\mu\nu}\,\tilde{W}^{A,\mu\nu} + C_{BB}\,\frac{\alpha_1}{4\pi}\,\frac{a}{f}\, B^{\mu\nu}\,\tilde{B}^{\mu\nu} + \mathcal{L}_{SM}\end{aligned} \tag{2.2}$$

with the ALP scalar field a, the ALP bare mass $m_{a,0}$, the fermion field ψ_F for all fermions F, the ALP couplings to the gauge fields $C_{GG,WW,BB}$ and the ALP-fermion coupling $\boldsymbol{C}_F$. The field-strength tensors of $\mathrm{SU}(3)_c$, $\mathrm{SU}(2)_L$ and $\mathrm{U}(1)_Y$ are $G^a_{\mu\nu}$, $W^A_{\mu\nu}$ and $B^{\mu\nu}$ with their coupling parameters $\alpha_s = g_s^2/(4\pi)$, $\alpha_2 = g^2/(4\pi)$ and $\alpha_1 = g'^2/(4\pi)$. The dual field strength tensors are denoted as $\tilde{V}^{\mu\nu} = \frac{1}{2}\,\epsilon^{\mu\nu\alpha\beta} V_{\alpha\beta}$ with

V = B, W, G. [12] The Feynman rules derived from this Lagrangian can be found in Appendix A.

2.2 The redundant Higgs operator

In addition to the Lagrangian in Equation 2.2 there is another common Lagrangian that is used, for example, in Reference [13]. It includes the ALP-Higgs term [12]

$$C_\phi O_\phi = C_\phi \frac{\partial^\mu a}{f} (\phi^\dagger D_\mu \phi), \tag{2.3}$$

with the operator O_ϕ and the ALP-Higgs coupling C_ϕ to the Higgs doublet ϕ. The ALP-Higgs term (Equation 2.3) can be shifted away with the field redefinitions: [12]

$$\phi \to e^{iC_\phi \frac{a}{f}} \phi, \quad F \to e^{-i\beta_F C_\phi \frac{a}{f}} F \tag{2.4}$$

Under the field redefinition the ALP-Higgs coupling becomes:

$$C_\phi \frac{\partial^\mu a}{f} (\phi^\dagger D_\mu \phi) \to \mathit{DIM\ 6\ term} + \frac{1}{2}(v+h)^2 \, \frac{g_W}{\mathit{cos}\,\theta} \, Z_\mu \, C_\phi \, \frac{\partial^\mu a}{f} \tag{2.5}$$

The dimension-6 term can be neglected as our Lagrangian (Equation 2.2) only includes interactions up to dimension-5 order. The other term of Equation 2.5 cancels with the Standard Model Higgs kinetic term:

$$(D^\mu \phi)^\dagger \, D_\mu \phi \to (D^\mu \phi)^\dagger \, D_\mu \phi + \mathit{DIM\ 6\ term} - \frac{1}{2}(v+h)^2 \, \frac{g_W}{\mathit{cos}\,\theta} \, Z_\mu \, C_\phi \, \frac{\partial^\mu a}{f}. \tag{2.6}$$

Again, the dimension-6 term can be neglected. Combining Equations 2.5 and 2.6 after the field redefinition, the ALP coupling to the Higgs vanishes and the Standard Model Higgs term stays invariant. The Standard Model Yukawa terms are invariant under field the transformation provided [12]

$$\beta_u - \beta_Q = -1, \quad \beta_d - \beta_Q = 1, \quad \beta_e - \beta_L = 1, \quad 3\beta_Q + \beta_L = 0, \tag{2.7}$$

where Q refers to all left-handed quarks, u_i (d_i) are vectors in flavor space for the right-handed quarks in the up-sector (down-sector) and L_i (e_i) is the vector for the left-handed (right-handed) leptons.

The fermion kinetic term transforms as:

$$i \, \overline{\Psi} \, \gamma^\mu \, D_\mu \, \Psi \to i \, \overline{\Psi} \, \gamma^\mu \, D_\mu \Psi + C_\phi \, \beta_F \, \frac{\partial^\mu a}{f} \, \overline{\Psi} \, \gamma_\mu \, \Psi \tag{2.8}$$

The additional term has the same structure as the ALP fermion term, which stays invariant; therefore, it induces the shift:

$$\boldsymbol{C}_F \to \boldsymbol{C}_F + C_\phi \, \beta_F \mathbb{1} \tag{2.9}$$

The operator O_ϕ is indeed a redundant operator and can be completely shifted away.

2.3 ALP across the scales

Renormalization deals with ultraviolet divergencies by absorbing them into the definition of all fundamental parameters. Because different divergencies occur at different energy scales, the redefined parameters are then scale dependent. [14]

This section is based on Reference [12] and describes the evolution of the ALP couplings from the ALP cutoff scale Λ to the flavor scale μ_f, which is shown in a schematic diagram in Figure 2.1. The ALP couplings are defined at the ALP cutoff scale Λ and then evolved down to the scale of electroweak symmetry breaking μ_W, where they are rotated to the physical mass basis and matched to the Weak Effective Lagrangian (WET). Then the couplings are in steps evolved down to the confinement scale, integrating out all particles along the way.

The gauge interactions contribute at two-loop order and the Yukawa interactions at one-loop order (e.g. diagrams in Figure 2.2). [12]

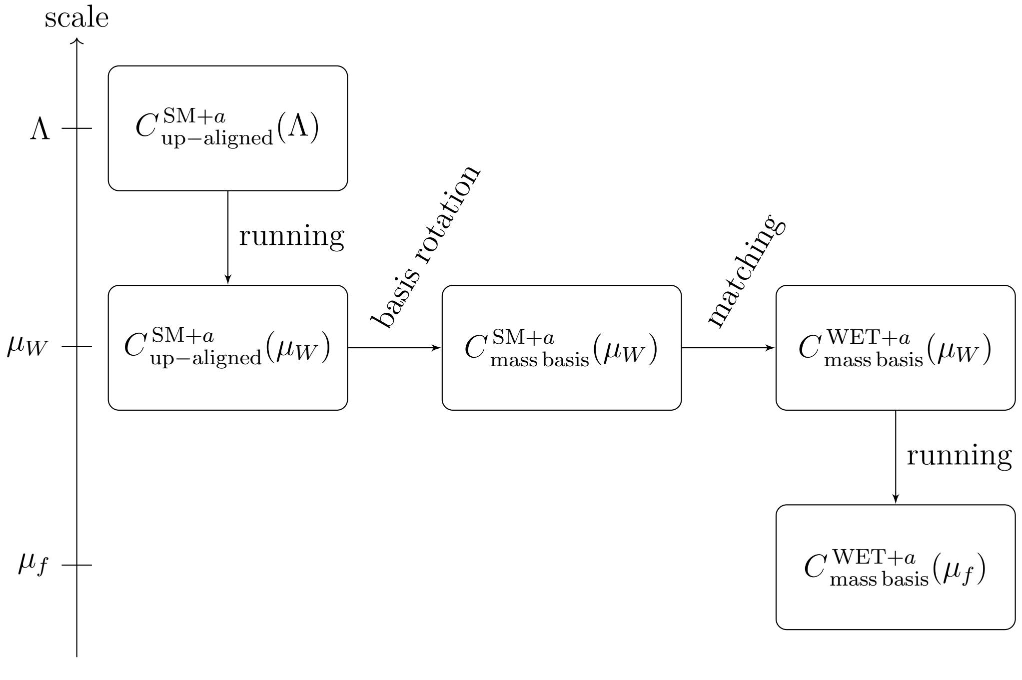

Figure 2.1: Schematic diagram of the ALP coupling evolution from the ALP cutoff scale Λ to the flavor scale μ_f.

2.3.1 Renormalization group evolution of the couplings down to the scale of electroweak symmetry breaking

For small ALP masses (order of the electroweak symmetry breaking scale = weak scale μ_W or less) the renormalization group (RG) equations evolve the Wilson coefficents down to the weak scale. The coupling to the gauge fields C_{GG}, C_{BB} and C_{WW} are scale independent. The RG evolution equations for the ALP couplings to fermions are: [12]

$$\begin{aligned}
\frac{\mathrm{d}}{\mathrm{d}\ln\mu}\boldsymbol{C}_Q(\mu) &= \frac{1}{32\pi^2}\left\{\boldsymbol{Y}_u\boldsymbol{Y}_u^\dagger + \boldsymbol{Y}_d\boldsymbol{Y}_d^\dagger, \boldsymbol{C}_Q\right\} \\
&\quad - \frac{1}{16\pi^2}\left(\boldsymbol{Y}_u\boldsymbol{C}_u\boldsymbol{Y}_u^\dagger + \boldsymbol{Y}_d\boldsymbol{C}_d\boldsymbol{Y}_d^\dagger\right) \\
&\quad + \left[\frac{\beta_Q}{8\pi^2}\,X - \frac{3\alpha_s^2}{4\pi^2}\,C_F^{(3)}\,\tilde{C}_{GG} \right. \\
&\qquad \left. - \frac{3\alpha_2^2}{4\pi^2}\,C_F^{(2)}\,\tilde{C}_{WW} - \frac{3\alpha_1^2}{4\pi^2}\,\mathcal{Y}_Q^2\,\tilde{C}_{BB}\right]\mathbb{1} \\
\frac{\mathrm{d}}{\mathrm{d}\ln\mu}\boldsymbol{C}_q(\mu) &= \frac{1}{16\pi^2}\left\{\boldsymbol{Y}_q^\dagger\boldsymbol{Y}_q, \boldsymbol{C}_q\right\} - \frac{1}{8\pi^2}\boldsymbol{Y}_q^\dagger\boldsymbol{C}_Q\boldsymbol{Y}_q \\
&\quad + \left[\frac{\beta_q}{8\pi^2}\,X + \frac{3\alpha_s^2}{4\pi^2}\,C_F^{(3)}\,\tilde{C}_{GG} + \frac{3\alpha_1^2}{4\pi^2}\,\mathcal{Y}_q^2\,\tilde{C}_{BB}\right]\mathbb{1} \\
\frac{\mathrm{d}}{\mathrm{d}\ln\mu}\boldsymbol{C}_L(\mu) &= \frac{1}{32\pi^2}\left\{\boldsymbol{Y}_e\boldsymbol{Y}_e^\dagger, \boldsymbol{C}_L\right\} - \frac{1}{16\pi^2}\boldsymbol{Y}_e\boldsymbol{C}_e\boldsymbol{Y}_e^\dagger \\
&\quad + \left[\frac{\beta_L}{8\pi^2}\,X - \frac{3\alpha_2^2}{4\pi^2}\,C_F^{(2)}\,\tilde{C}_{WW} - \frac{3\alpha_1^2}{4\pi^2}\,\mathcal{Y}_L^2\,\tilde{C}_{BB}\right]\mathbb{1} \\
\frac{\mathrm{d}}{\mathrm{d}\ln\mu}\boldsymbol{C}_e(\mu) &= \frac{1}{16\pi^2}\left\{\boldsymbol{Y}_e^\dagger\boldsymbol{Y}_e, \boldsymbol{C}_e\right\} - \frac{1}{8\pi^2}\boldsymbol{Y}_e^\dagger\boldsymbol{C}_L\boldsymbol{Y}_e \\
&\quad + \left[\frac{\beta_e}{8\pi^2}\,X + \frac{3\alpha_1^2}{4\pi^2}\,\mathcal{Y}_e^2\,\tilde{C}_{BB}\right]\mathbb{1}
\end{aligned} \tag{2.10}$$

The eigenvalue of the quadratic Casimir operator in the fundamental representation of SU(N) is given by: [12]

$$C_F^{(N)} = \frac{N^2-1}{2N} \tag{2.11}$$

The tilde gauge couplings are defined as: [12]

$$\begin{aligned}
\tilde{C}_{GG} &= C_{GG} + \frac{1}{2}\,\mathrm{Tr}(\boldsymbol{C}_u + \boldsymbol{C}_d - 2\,\boldsymbol{C}_Q) \\
\tilde{C}_{WW} &= C_{WW} - \frac{1}{2}\,\mathrm{Tr}(3\,\boldsymbol{C}_Q + \boldsymbol{C}_L) \\
\tilde{C}_{BB} &= C_{BB} + \,\mathrm{Tr}\left(\frac{4}{3}\,\boldsymbol{C}_u + \frac{1}{3}\,\boldsymbol{C}_d - \frac{1}{6}\,\boldsymbol{C}_Q - \frac{1}{2}\,\boldsymbol{C}_L\right)
\end{aligned} \tag{2.12}$$

These tilde gauge couplings are used in an equivalent alternative effective Lagrangian whith the ALP-fermion couplings written in terms of the Yukawa interactions: [12]

$$\begin{aligned}\mathcal{L}_{\text{eff}}^{D\leq 5} = \frac{1}{2}\left(\partial_\mu a\right)\left(\partial^\mu a\right) - \frac{m_{a,0}^2}{2}\, a^2 \\ - \frac{a}{f}\left(\overline{Q}\,\phi\,\tilde{\boldsymbol{Y}}_d\, d_R + \overline{Q}\,\tilde{\phi}\,\tilde{\boldsymbol{Y}}_u\, u_R + \overline{L}\,\phi\,\tilde{\boldsymbol{Y}}_e\, e_R + \text{h.c.}\right) \\ + \tilde{C}_{GG}\,\frac{\alpha_s}{4\pi}\,\frac{a}{f}\, G_{\mu\nu}^a\,\tilde{G}^{a,\mu\nu} + \tilde{C}_{WW}\,\frac{\alpha_2}{4\pi}\,\frac{a}{f}\, W_{\mu\nu}^A\,\tilde{W}^{A,\mu\nu} \\ + \tilde{C}_{BB}\,\frac{\alpha_1}{4\pi}\,\frac{a}{f}\, B^{\mu\nu}\,\tilde{B}^{\mu\nu}\end{aligned} \tag{2.13}$$

The tilde Yukawa interactions are defined as follows: [12]

$$\begin{aligned}\tilde{\boldsymbol{Y}}_d &= i\left(\boldsymbol{Y}_d C_d - C_Q \boldsymbol{Y}_d\right) \\ \tilde{\boldsymbol{Y}}_u &= i\left(\boldsymbol{Y}_u C_u - C_Q \boldsymbol{Y}_u\right) \\ \tilde{\boldsymbol{Y}}_e &= i\left(\boldsymbol{Y}_e C_e - C_L \boldsymbol{Y}_e\right)\end{aligned} \tag{2.14}$$

X is defined as [12]

$$X = \text{Tr}\Big[3\boldsymbol{C}_Q\left(\boldsymbol{Y}_u\boldsymbol{Y}_u^\dagger - \boldsymbol{Y}_d\boldsymbol{Y}_d^\dagger\right) - 3\boldsymbol{C}_u\boldsymbol{Y}_u^\dagger\boldsymbol{Y}_u + 3\boldsymbol{C}_d\boldsymbol{Y}_d^\dagger\boldsymbol{Y}_d - \boldsymbol{C}_L\boldsymbol{Y}_e\boldsymbol{Y}_e^\dagger + \boldsymbol{C}_e\boldsymbol{Y}_e^\dagger\boldsymbol{Y}_e\Big], \tag{2.15}$$

which contains the two-loop gauge boson interactions and the contribution of a UV-divergent graph, which requires the redundant operator O_ϕ as a counterterm. Both graphs are shown in Figure 2.2. [12]

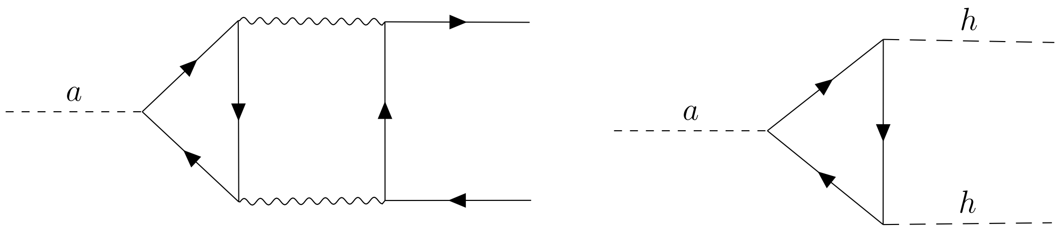

Figure 2.2: The first diagram shows the two-loop gauge contribution. The second diagram shows a UV-divergent contribution, which cancels with the vertex from the redundant operator O_ϕ.

The terms in Equation 2.10 proportional to the ALP-gauge couplings stem from the contributions shown in Figure 2.3. [12]

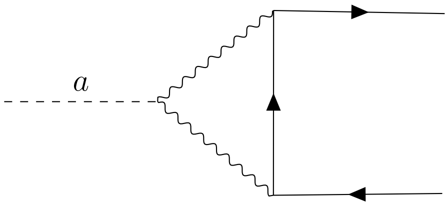

Figure 2.3: One-loop gauge contributions to the running.

The remaining terms proportional to Yukawa interactions are contributions from the diagrams shown in Figure 2.4. [12]

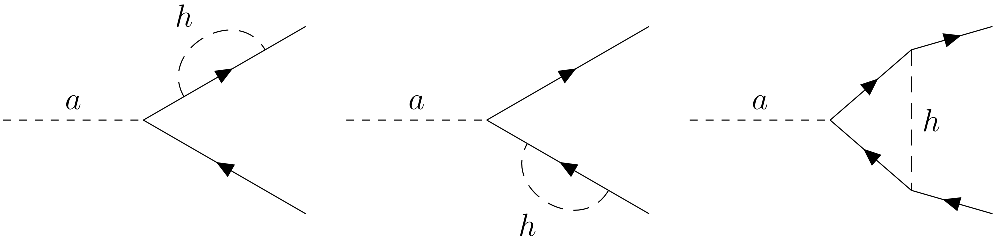

Figure 2.4: Running contributions proportional to the Yukawa interactions.

The Yukawa matrices are choosen to be diagonal in the up- and lepton sector and all Yukawa couplings except $y_t \approx 1$ are neglected, the RG equations simplify to the following expressions: [12]

$$\begin{aligned}
\frac{\mathrm{d}}{\mathrm{d}\ln\mu}\left[C_Q(\mu)\right]_{ii} &= -\frac{y_t^2}{8\pi^2}\left(\frac{\delta_{i3}}{2}+3\beta_Q\right)C_{tt} - \frac{\alpha_s^2}{\pi^2}\tilde{C}_{GG} - \frac{9\alpha_2^2}{16\pi^2}\tilde{C}_{WW} - \frac{\alpha_1^2}{48\pi^2}\tilde{C}_{BB} \\
\frac{\mathrm{d}}{\mathrm{d}\ln\mu}\left[C_Q(\mu)\right]_{ij} &= \frac{y_t^2}{32\pi^2}\left(\delta_{i3}+\delta_{j3}\right)\left(C_Q\right)_{ij}; \qquad i \neq j \\
\frac{\mathrm{d}}{\mathrm{d}\ln\mu}\left[C_u(\mu)\right]_{ii} &= \frac{y_t^2}{8\pi^2}\left(\delta_{i3}-3\beta_u\right)C_{tt} + \frac{\alpha_s^2}{\pi^2}\tilde{C}_{GG} + \frac{\alpha_1^2}{3\pi^2}\tilde{C}_{BB} \\
\frac{\mathrm{d}}{\mathrm{d}\ln\mu}\left[C_u(\mu)\right]_{ij} &= \frac{y_t^2}{16\pi^2}\left(\delta_{i3}+\delta_{j3}\right)\left(C_u\right)_{ij}; \qquad i \neq j \\
\frac{\mathrm{d}}{\mathrm{d}\ln\mu}\left[C_d(\mu)\right]_{ij} &= \delta_{ij}\left(-\frac{3y_t^2}{8\pi^2}\beta_d C_{tt} + \frac{\alpha_s^2}{\pi^2}\tilde{C}_{GG} + \frac{\alpha_1^2}{12\pi^2}\tilde{C}_{BB}\right) \\
\frac{\mathrm{d}}{\mathrm{d}\ln\mu}\left[C_L(\mu)\right]_{ij} &= \delta_{ij}\left(-\frac{3y_t^2}{8\pi^2}\beta_L C_{tt} - \frac{9\alpha_2^2}{16\pi^2}\tilde{C}_{WW} - \frac{3\alpha_1^2}{16\pi^2}\tilde{C}_{BB}\right) \\
\frac{\mathrm{d}}{\mathrm{d}\ln\mu}\left[C_e(\mu)\right]_{ij} &= \delta_{ij}\left(-\frac{3y_t^2}{8\pi^2}\beta_e C_{tt} + \frac{3\alpha_1^2}{4\pi^2}\tilde{C}_{BB}\right)
\end{aligned} \tag{2.16}$$

with the ALP coupling to the physical top mass eigenstate [12]

$$C_{tt}(\mu) = [C_u(\mu)]_{33} - [C_Q(\mu)]_{33}\,. \tag{2.17}$$

This equation can be generalized to other ALP-fermion couplings. It can be seen from Equation 2.17 that the ALP couples to the axial vector current $\overline{\psi}\gamma_\mu\gamma_5\psi$. The combination of the coupling to the right-handed minus left-handed top current adds a γ_5 through the chiral projection operators $P_{R/L} = \frac{1}{2}(1 \pm \gamma_5)$ to the ALP fermion coupling in Equation 2.2, resulting in a coupling to the axial vector current.

2.3.2 Rotation to the mass basis

At the weak scale and below a basis rotation is performed to express the couplings in the mass eigenstates of physical particles. This basis is then maintained for the lower scales. Therefore, the down sector is rotated by the CKM matrix $\mathbf{V}$: [12]

$$\boldsymbol{C}_D = \mathbf{V}^\dagger \boldsymbol{C}_Q \mathbf{V} \tag{2.18}$$

The ALP couplings to photons and Z bosons can be expressed as a function of the C_{WW} and C_{BB} coupling: [12]

$$\begin{aligned} C_{WW} &= C_{WW} \\ C_{\gamma\gamma} &= C_{WW} + C_{BB} \\ C_{\gamma Z} &= \cos^2(\theta_w)\, C_{WW} - \sin^2(\theta_w)\, C_{BB} \\ C_{ZZ} &= \cos^4(\theta_w)\, C_{WW} + \sin^4(\theta_w)\, C_{BB} \end{aligned} \tag{2.19}$$

2.3.3 Matching at the weak scale

At the weak scale μ_W the Lagrangian 2.2 is matched to the Lagrangian of the effective theory of weak interaction where the W, Z and Higgs boson and the top quark quark are integrated out: [12]

$$\begin{aligned} \mathcal{L}_{\text{eff}}^{D\leq 5}(\mu \lesssim \mu_w) = \frac{1}{2}(\partial_\mu a)(\partial^\mu a) - \frac{m_{a,0}^2}{2}a^2 + \mathcal{L}'_{\text{ferm}}(\mu) \\ + C_{GG}\frac{\alpha_s}{4\pi}\frac{a}{f}G^a_{\mu\nu}\tilde{G}^{\mu\nu,a} + C_{\gamma\gamma}\frac{\alpha}{4\pi}\frac{a}{f}F_{\mu\nu}\tilde{F}^{\mu\nu} \end{aligned} \tag{2.20}$$

$$\begin{aligned} \mathcal{L}'_{\text{ferm}}(\mu) = \frac{\partial^\mu a}{f}\big(&\overline{u}_{L,i}[C_U]_{ij}\gamma_\mu u_{L,j} + \overline{u}_{R,i}[C_u]_{ij}\gamma_\mu u_{R,j} + \overline{d}_L \boldsymbol{C}_D\gamma_\mu d_L \\ &+ \overline{d}_R \boldsymbol{C}_d \gamma_\mu d_R + \overline{\nu}_L \boldsymbol{C}_\nu \gamma_\mu \nu_L + \overline{e}_L \boldsymbol{C}_E \gamma_\mu e_L + \overline{e}_R \boldsymbol{C}_e \gamma_\mu e_R\big) \\ &\text{for } i,j \in \{1,2\} \end{aligned} \tag{2.21}$$

$[C_U]_{ij}$ ($[C_u]_{ij}$) is the ALP coupling to left- (right-)handed up-sector, $[C_D]_{ij}$ ($[C_d]_{ij}$) is the ALP coupling to left- (right-)handed down-sector, $[C_E]_{ij}$ ($[C_e]_{ij}$) is the ALP coupling to left- (right-)handed electron, muon and tauon. $[C_\nu]_{ij}$ is the ALP coupling to neutrinos. The matching contributions to the gauge couplings are suppressed by the mass scale m_a^2/m_t^2 and m_a^2/m_W^2 and can be neglected for a light ALP. [12] The matching contributions to the ALP-fermion couplings are: [12]

$$\begin{aligned}
\Delta \boldsymbol{C}_F(\mu_w) = {} & \frac{3y_t^2}{8\pi^2} C_{tt} \left(T_3^F - Q_F s_w^2\right) \ln \frac{\mu_W^2}{m_t^2} \mathbb{1} \\
& + \frac{3\alpha^2}{8\pi^2} \left[\frac{C_{WW}}{2s_w^4} \left(\ln \frac{\mu_W^2}{m_W^2} + \frac{1}{2} + \delta_1 \right) \right. \\
& \qquad + \frac{2C_{\gamma Z}}{s_w^2 c_w^2} Q_F \left(T_3^F - Q_F s_w^2\right) \left(\ln \frac{\mu_W^2}{m_Z^2} + \frac{3}{2} + \delta_1 \right) \\
& \qquad \left. + \frac{C_{ZZ}}{s_w^4 c_w^4} \left(T_3^F - Q_F s_w^2\right)^2 \left(\ln \frac{\mu_W^2}{m_Z^2} + \frac{1}{2} + \delta_1 \right) \right] \mathbb{1} \\
& + \delta_{FD}\, \hat{\Delta} \boldsymbol{C}_D(\mu_w)
\end{aligned} \tag{2.22}$$

$$\begin{aligned}
\Delta \boldsymbol{C}_f(\mu_w) = {} & \frac{3y_t^2}{8\pi^2} C_{tt} \left(-Q_f s_w^2\right) \ln \frac{\mu_W^2}{m_t^2} \mathbb{1} \\
& + \frac{3\alpha^2}{8\pi^2} Q_f^2 \left[\frac{2C_{\gamma Z}}{c_w^2} \left(\ln \frac{\mu_W^2}{m_Z^2} + \frac{3}{2} + \delta_1 \right) \right. \\
& \qquad \left. - \frac{C_{ZZ}}{c_w^4} \left(\ln \frac{\mu_W^2}{m_Z^2} + \frac{1}{2} + \delta_1 \right) \right] \mathbb{1}
\end{aligned} \tag{2.23}$$

$$\begin{aligned}
& [\hat{\Delta} C_D(\mu_w)]_{ij} = \\
& \quad = \frac{y_t^2}{16\pi^2} \left\{ V_{mi}^* V_{nj} [C_U(\mu_w)]_{mn} (\delta_{m3} + \delta_{n3}) \right. \\
& \qquad \qquad \cdot \left[-\frac{1}{4} \ln \frac{\mu_w^2}{m_t^2} - \frac{3}{8} + \frac{3}{4} \frac{1 - x_t + \ln x_t}{(1 - x_t)^2} \right] \\
& \qquad + V_{3i}^* V_{3j} [C_U(\mu_w)]_{33} \\
& \qquad + V_{3i}^* V_{3j} [C_u(\mu_w)]_{33} \left[\frac{1}{2} \ln \frac{\mu_w^2}{m_t^2} - \frac{1}{4} - \frac{3}{2} \frac{1 - x_t + \ln x_t}{(1 - x_t)^2} \right] \\
& \qquad \left. - \frac{3\alpha}{2\pi s_w^2} C_{WW}\, V_{3i}^* V_{3j} \, \frac{1 - x_t + x_t \ln x_t}{(1 - x_t)^2} \right\}
\end{aligned} \tag{2.24}$$

The contribution diagrams are shown in Figure 2.5. Diagram a) shows the contribution to Equation 2.22 for the first term with the ALP-top couplings C_{tt} and the Z boson term $T_3^F - Q_F s_w^2$. The terms in Equation 2.22 and 2.23 proportional to the ALP-gauge couplings stem from diagram b) of 2.5. Equation 2.24 contains off-diagonal matching contributions for the down quark sector which lead to flavor-changing neutral currents (FCNC) even for flavor-diagonal ALP couplings at the cutoff scale Λ. Its contributions stem from the diagrams c) and d) where the combination of a W boson and virtual top quarks are the only non-zero contributions. The term proportional to the C_{WW} coupling arises from diagram b) for a W boson with a virtual top quark. [12]

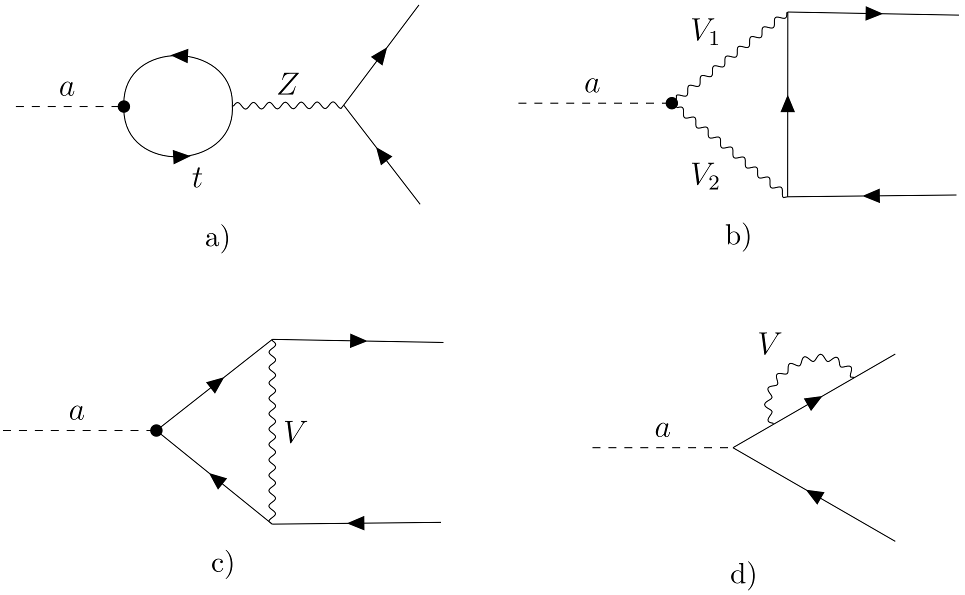

a) b) c) d)

Figure 2.5: One-loop matching contributions to the ALP-fermion couplings. The diagrams a) and b) give rise to the flavor-diagonal matching contributions, the diagrams c) and d) and diagram b) with W bosons and a virtual top quark give rise to flavor off-diagonal matching contributions in the down-quark sector. [12]

2.3.4 Running from the weak scale to the confinement scale

Below the weak scale μ_W the Yukawa contributions as well as the W and Z boson are integrated out. The contributions to the RG evolution equations of the fermions come from photons and gluons: [12]

$$\begin{aligned} \frac{\mathrm{d}}{\mathrm{d}\ln\mu}\boldsymbol{C}_q(\mu) &= -\frac{\mathrm{d}}{\mathrm{d}\ln\mu}\boldsymbol{C}_Q(\mu) = \left(\frac{\alpha_s^2}{\pi^2}\,\tilde{C}_{GG} + \frac{3\,\alpha^2}{4\pi^2}Q_q^2\,\tilde{C}_{\gamma\gamma}\right)\mathbb{1} \\ \frac{\mathrm{d}}{\mathrm{d}\ln\mu}\boldsymbol{C}_e(\mu) &= -\frac{\mathrm{d}}{\mathrm{d}\ln\mu}\boldsymbol{C}_E(\mu) = \frac{3\,\alpha^2}{4\pi^2}\,\tilde{C}_{\gamma\gamma}\,\mathbb{1} \end{aligned} \tag{2.25}$$

The remaining contributions stem from diagrams 2.3 and the first diagram of Figure 2.2 with photons and gluons as the only contributing gauge bosons. [12] At the confinement scale of $\mu = 1$ GeV the Lagrangian can further be matched to the chiral Lagrangian because the remaining quarks u, d and s hadronize. [12]

3 Methods

This section gives an introduction into the methods which have been used for all our analyses, the treatment of statistics in the high energy observables and the implementation of the renormalization group equations. More specific methods are described in the individual phenomenology sections.

3.1 Statistical framework

Our aim is to constrain the couplings $C_{GG}(\Lambda)$ and $C_{ff}(\Lambda)$. Therefore, we evaluate their influence on experimental observables. To find and justify such bounds we apply a specific statistical treatment, which considers the experimental data, our predictions and experimental and theoretical errors. Thus we need to be able to calculate a likelihood ratio function $\lambda(\alpha)$ for any specific point $\alpha = (C_{GG}(\Lambda), C_{ff}(\Lambda))$ in the parameter space which quantifies how reasonable it would be to accept such parameters. [15] By that we can then set a threshold corresponding to a specific confidence level (CL) in a Gaussian distribution.

The likelihood function $\mathcal{L}(\alpha|x)$ returns the plausibility for a parameter choice $\alpha = (C_{GG}(\Lambda), C_{ff}(\Lambda))$ given that an observable x has been measured. As such a function is hard to construct by itself, we first consider the opposite, a probability density function $p(x|\alpha)$ for a given model and known parameters α. If $p(x|\alpha)$ is integrated over an interval $[x_1, x_2]$ it gives the probability for measuring some value within the interval. Locally, $p(x|\alpha)\,\mathrm{d}x$ describes the probability for observing a value in the small region $[x, x + \mathrm{d}x]$. $p(x|\alpha)$ is normalized, so that the overall probability $\int_{-\infty}^{\infty} p(x|\alpha)\,\mathrm{d}x$ is always 1. Starting from a known measurement x, we can use the same values $\mathcal{L}(\alpha|x) = p(x|\alpha)$ as a reasonable measure and treat α as the variable we scan over while keeping x fixed. This function's integral is not normalized to 1. [15]

The likelihood is most advantageously used in the form of the likelihood ratio function $\lambda(\alpha|x)$: [15, 16]

$$\lambda(\alpha|x) = -2\ln\left(\frac{\mathcal{L}(\alpha|x)}{\sup_{\alpha'} \mathcal{L}(\alpha'|x)}\right) \tag{3.1}$$

Here, $\sup_{\alpha'} \mathcal{L}(\alpha'|x)$ describes the supremum of the likelihood for any α' of the parameter space. This equation takes the logarithm of $\mathcal{L}$, so that products decompose into sums, flips it, so that unlikely regions correspond to large values and shifts it vertically. This shift normalizes the likelihood ratio such that $\lambda(\alpha_{\text{best}}|x) \overset{!}{=} 0$ for the best fit(s) α_{best} and $\lambda(\alpha|x) > 0$ otherwise. Wilks' theorem states that this likelihood ratio is $\chi^2(\Delta n)$-distributed with Δn being the amount of parameters we scan over ($\Delta n = 2$ in our analysis). The theorem requires a large enough sample size, which is satisfied in our setups. [15, 16] Therefore, in a purely Gaussian case, we can equate the 68 % CL, corresponding to the 1σ bounds for a Gaussian distribution, with the value of $\Delta\chi^2 \coloneqq \lambda(\alpha|x) = 2.3$. Analogly, we find the 95 % CL, corresponding to the Gaussian 2σ bounds, at the value of $\Delta\chi^2 = \lambda(\alpha|x) = 5.9$. [17]

Theoretical, statistic and systematic errors all lead to different types of probability distributions and likelihood functions. The different types are summarized in the following. [15]

Collider experiments produce a large number of collisions while each collision has a tiny probability for an event of interest, leading to d observed events in the end. This statistical setting leads, even in perfect reproducibility and control of all experimental parameters, to statistical errors following a Poisson distribution. Thus the observed number of events d follow the probability mass function $p_{\text{Poiss}}(d|\tilde{d})$ with the expected amount of events $\tilde{d}$: [15]

$$p_{\text{Poiss}}(d|\tilde{d}) = \frac{\tilde{d}^d}{d!} e^{-\tilde{d}} \tag{3.2}$$

The likelihood function is then the same expression $\mathcal{L}_{\text{Poiss}}(\tilde{d}|d) = p_{\text{Poiss}}(d|\tilde{d})$, taking $\tilde{d}$ as the variable. [15]

As any experiment relies on many parameters which can't be measured or controlled exactly, the number of measured events underlies systematic errors σ_{sys}. These typically contribute by creating a Gaussian distribution: [15]

$$p_{\text{Gauss}}(d|\tilde{d}) = \frac{1}{\sqrt{2\pi}\sigma_{\text{sys}}} \exp\left(-\frac{(d-\tilde{d})^2}{2\sigma_{\text{sys}}^2}\right) \tag{3.3}$$

The probability is now written in terms of all systematic errors $\sigma_{d,i}$ and equated with the likelihood. By logarithmizing it simplifies to

$$-2\ln\mathcal{L}_{\text{Gauss}}(\tilde{d}|d) = \frac{(d-\tilde{d})^2}{\sum_{\text{sys}} \sigma_{d,i}^2} + C, \tag{3.4}$$

where $C = \ln\left(2\pi \sum_{\text{sys}} \sigma_{d,i}^2\right)$ is only a constant offset. [15] This expression is minimal for $d = \tilde{d}$ where it is zero if we neglect C and then equivalent to the likelihood ratio $\lambda_{\text{Gauss}}(\tilde{d}|d)$. [15]

Theoretical uncertainties are modeled as flat distributions: [15]

$$\mathcal{L}_{\text{Flat}}(\tilde{d}|d) \propto \begin{cases} 1 & \text{for } \left|d-\tilde{d}\right| \leq \sigma_{\text{theo}} \\ 0 & \text{for } \left|d-\tilde{d}\right| > \sigma_{\text{theo}} \end{cases} \tag{3.5}$$

They allow for a limited deviation $|d-\tilde{d}|$ between the measurement and the model, which are indifferently accepted. Above the threshold σ_{theo} the difference is considered significant and the model $\tilde{d}$ is excluded. They can be combined with the experimental errors into one likelihood ratio: [15]

$$\lambda_{\text{Gauss+Flat}}(\tilde{d}|d) = \Delta\chi^2 = \begin{cases} \frac{\left(\tilde{d}-d+\sigma_{\text{theo}}\right)^2}{\sigma_{\text{sys}}^2} & \text{for } \tilde{d}-d < -\sigma_{\text{theo}} \\ 0 & \text{for } \left|\tilde{d}-d\right| \leq \sigma_{\text{theo}} \\ \frac{\left(\tilde{d}-d-\sigma_{\text{theo}}\right)^2}{\sigma_{\text{sys}}^2} & \text{for } \tilde{d}-d > +\sigma_{\text{theo}} \end{cases} \tag{3.6}$$

This function is a parabola that is cut open at its minimum, so that its branches start at $\tilde{d}-d = \pm\sigma_{\text{theo}}$ and in between it is constant at its minimum of $\lambda = 0$. This allows for a small deviation which doesn't lead to an increase of λ. [15]

Finally, all these distributions have to be summarized into one likelihood function. Here we use the approximate formula: [15]

$$\frac{1}{\ln\mathcal{L}} = \frac{1}{\ln\mathcal{L}_{\text{Poiss}}} + \frac{1}{\ln\mathcal{L}_{\text{Gauss+Flat}}} \tag{3.7}$$

We are now able to calculate a likelihood for any point $\alpha = (C_{GG}(\Lambda), C_{ff}(\Lambda))$ in our parameter space. Using that, we search for the bounds of the excluded area in the parameter space with $\Delta\chi^2 = \lambda(\alpha|x) > 2.3$ or 5.9, respectively. For the sampling we use Markov Chains to be able to expand our fit for future work with more parameters. The sampling with two parameters is also possible with a simple grid scan. The whole process is implemented in the `sfitter` framework [18], which has already been used for similar fits. [15, 19, 20]

3.2 Implementation of the renormalization group equations

We implemented the renormalization group equations (Section 2.3) to solve the coupled differential equations numerically. This allows us to both evolve ALP couplings down from set values at the cutoff scale Λ as well as evolving the bounds on couplings e.g. at the m_t scale up to the cutoff scale. Thereby we can combine measurements at different scales. We work consistently at one-loop order. A workflow diagram is shown in Figure 3.1.

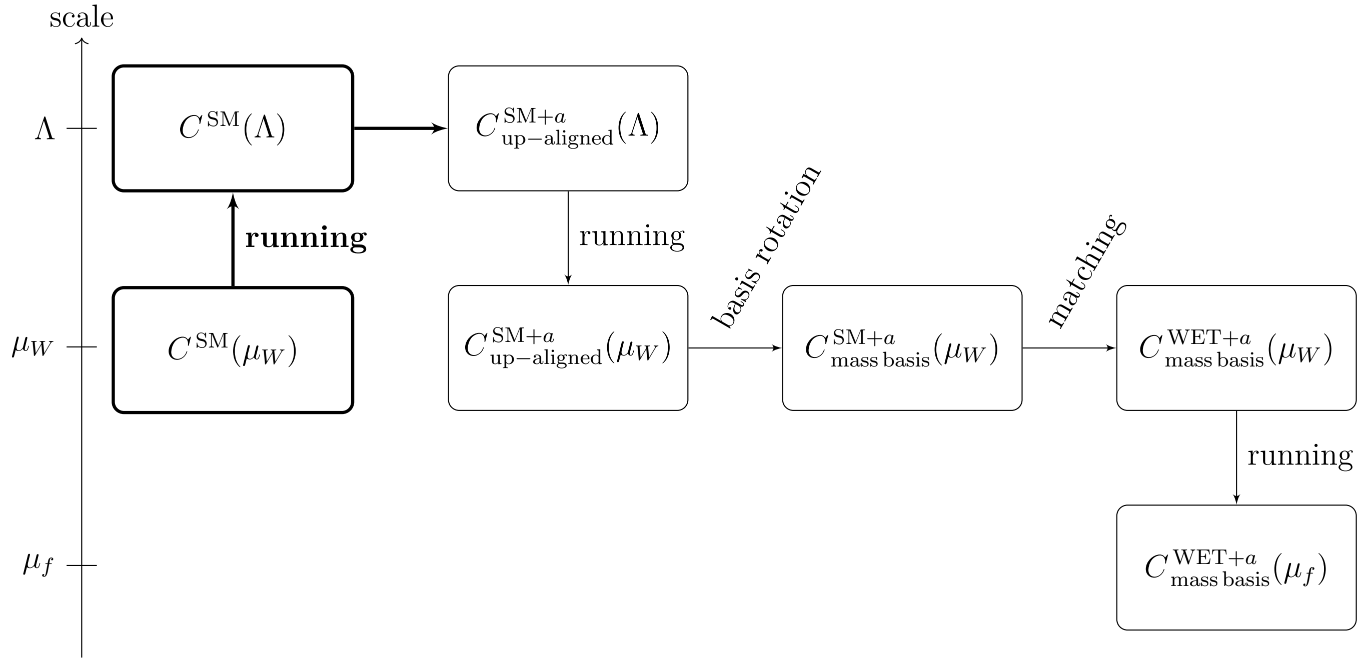

Figure 3.1: Schematic diagram of the workflow of our implementation of the renormalization group equations from Section 2.3. The Standard Model parameters are first evolved to the ALP cutoff scale $\Lambda = 4\pi f$, and then further evolved together with the ALP couplings.

First, the Standard Model parameters given at $\mu = m_Z$ are evolved to the ALP cutoff scale Λ. These parameters are inputs for the ALP renormalization group equations and this way ensures that these input parameters are always at the same scale as the ALP model. Then both the ALP couplings as well as the Standard Model parameters are evolved down to the matching scale $\mu_W = m_Z$. Subsequently, the ALP and Standard Model parameters are evolved down to the confinement scale of 1 GeV. Here, all the particles are integrated out as soon as the scale is below their mass. The running below the confinement scale is very weak; therefore, it was neglected.

4 Phenomenology of ALPs

Our analysis constrains the ALP couplings $C_{GG}(\Lambda)$, $C_{ff}(\Lambda)$ and $C_{WW}(\Lambda)$ and is the first analysis to do this first step towards a global fit. As ALP couplings are interrelated through the renormalization group equations (see Section 2.3) a coupling which is set to zero at the cutoff scale Λ can acquire a nonzero value at lower scales through running and matching contributions. To understand the connection between the couplings it is necessary to study a set of ALP couplings. By comparing our predictions with the ALP model to current measurements the couplings can be constrained. Our analysis combines high energy and flavor observables. As the $t\bar{t}$ production only constrains the product $C_{ff}(\Lambda) \cdot C_{GG}(\Lambda)$, it leaves blind directions for low values of either of the couplings. The $t\bar{t}t\bar{t}$ production and the dijet angular distribution, the latter confining only the $C_{GG}(\Lambda)$ coupling, are used to resolve these blind directions. The B-meson decay constrains $C_{WW}(\Lambda)$ and $C_{ff}(\Lambda)$. With the implementation of the ALP evolution across the scales (Section 3.2) the results can be evolved to the ALP cutoff scale Λ and combined. We assume flavor alignment at the cutoff scale Λ, which means that all flavor diagonal couplings are set to the same non-zero value.

4.1 ALPs in $t\bar{t}$ production

As the ALP-fermion coupling is expected to be Yukawa dependent (see Section 2.3) it seems promising to study ALP-top processes. At tree-level in pp collisions the ALP is produced via gluon gluon fusion. In this section we study the effect of ALP exchange in $t\bar{t}$ production to constrain the product of the couplings $C_{GG}(\Lambda) \cdot C_{ff}(\Lambda)$.

4.1.1 Theory

Figure 4.1 shows an exemplary Feynman diagram describing the $t\bar{t}$ production process in the Standard Model and the additional $t\bar{t}$ production process in the ALP model, respectively.

Figure 4.1: Feynman diagrams for $t\bar{t}$ production with the s-channel Standard Model process (left) and the ALP process (right).

The ALP as a color singlet couples differently than the color octet gluon which accounts for different amplitudes.

The amplitude squared for $t\bar{t}$ production has been calculated with the Feynman rules in Appendix A to be

$$\begin{aligned} |\bar{\mathcal{M}}|^2 = & \ |\bar{\mathcal{M}}_{SM}|^2 + \frac{s^3 m_t^2 \alpha_s^2}{4f^2 \left(m_t^2 - t\right)\left(m_a^2 - s\right)\left(m_t^2 - u\right)} C_{GG} \left(C_Q^{(3,3)} - C_u^{(3,3)}\right) \\ & + \frac{3 s^3 m_t^2 \alpha_s^2}{32\pi^2 f^4 \left(m_a^2 - s\right)^2} C_{GG}^2 \left(C_Q^{(3,3)} - C_u^{(3,3)}\right)^2 \end{aligned} \tag{4.1}$$

or, equivalently, when expressed with the scattering angle θ between the top quarks

$$\begin{aligned} |\bar{\mathcal{M}}|^2 = & \ |\bar{\mathcal{M}}_{SM}|^2 \\ & + \frac{s^2 m_t^2 \alpha_s^2}{f^2 \left(m_a^2 - s\right)\left(4 m_t^2 \cos^2\theta - s \cos^2\theta + s\right)} C_{GG} \left(C_Q^{(3,3)} - C_u^{(3,3)}\right) \\ & + \frac{3 s^3 m_t^2 \alpha_s^2}{32\pi^2 f^4 \left(m_a^2 - s\right)^2} C_{GG}^2 \left(C_Q^{(3,3)} - C_u^{(3,3)}\right)^2 . \end{aligned} \tag{4.2}$$

The amplitude squared in the Standard Model is:

$$
\begin{aligned}
&|\bar{\mathcal{M}}_{SM}|^2 = \\
&\quad = -\Big[\pi^2\alpha_s^2\big(m_t^4\left(3t^2+14tu+3u^2\right)-m_t^2\left(7t^2u+t^3+7tu^2+u^3\right) \\
&\qquad\quad -6m_t^8+tu\left(t^2+u^2\right)\big)\cdot\big(18m_t^2(t+u)-18m_t^4+s^2 \\
&\qquad\qquad\qquad -9\left(t^2+u^2\right)\big)\Big]\Big/\Big[3s^2\left(t-m_t^2\right)^2\left(u-m_t^2\right)^2\Big] \\
&\quad = -\Big[\pi^2\alpha_s^2\big(s\left(9\cos^2(\theta)+7\right)-36\cos^2(\theta)m_t^2\big) \\
&\qquad\quad \big(-8s\sin^2(\theta)m_t^2-8m_t^2\left(4\cos^2(\theta)m_t^2+s\cos^4(\theta)\right) \\
&\qquad\quad +16\cos^4(\theta)m_t^4+32m_t^4 \\
&\qquad\qquad +s^2\left(\cos^4(\theta)-1\right)\big)\Big]\Big/\Big[3s\left(4\cos^2(\theta)m_t^2+s\sin^2(\theta)\right)^2\Big]
\end{aligned}
\tag{4.3}
$$

In equations 4.1, 4.2 and 4.3 the Mandelstam variables are denoted by s, t, u and m_t is the top mass.

4.1.2 Methods

The ALP model was implemented into Madgraph5_aMC@NLO [21] using a UFO model file created with FeynRules [22]. The parton distribution function (pdf) set `nnpdf31_NLO_as_0118` [23] was used. This pdf set is not based on top quark experiments so we can avoid correlations in the top-sector.

Alongside the ATLAS measurement of the production cross section of $\sigma = (826.4 \pm 3.6(stat) \pm 11.5(syst) \pm 15.7(lumi) \pm 1.9(beam))$ pb [24], the bins $10, 12, 14, 16$ (highest bins, skipping every other bin to avoid the use of a correlation matrix) of the normalized CMS measurement of the leptonic transverse momentum p_t [25] were used as measurements with which the model predictions were compared.

As a theoretical uncertainty for our LO predictions we assumed double the theoretical uncertainty of the NLO predictions of Reference [25]. The experimental data, the Standard Model predictions from Reference [25] and theoretical data and uncertainties were used for our `sfitter` [18] analysis, the statistical framework of which is described in Section 3.1.

4.1.3 Results

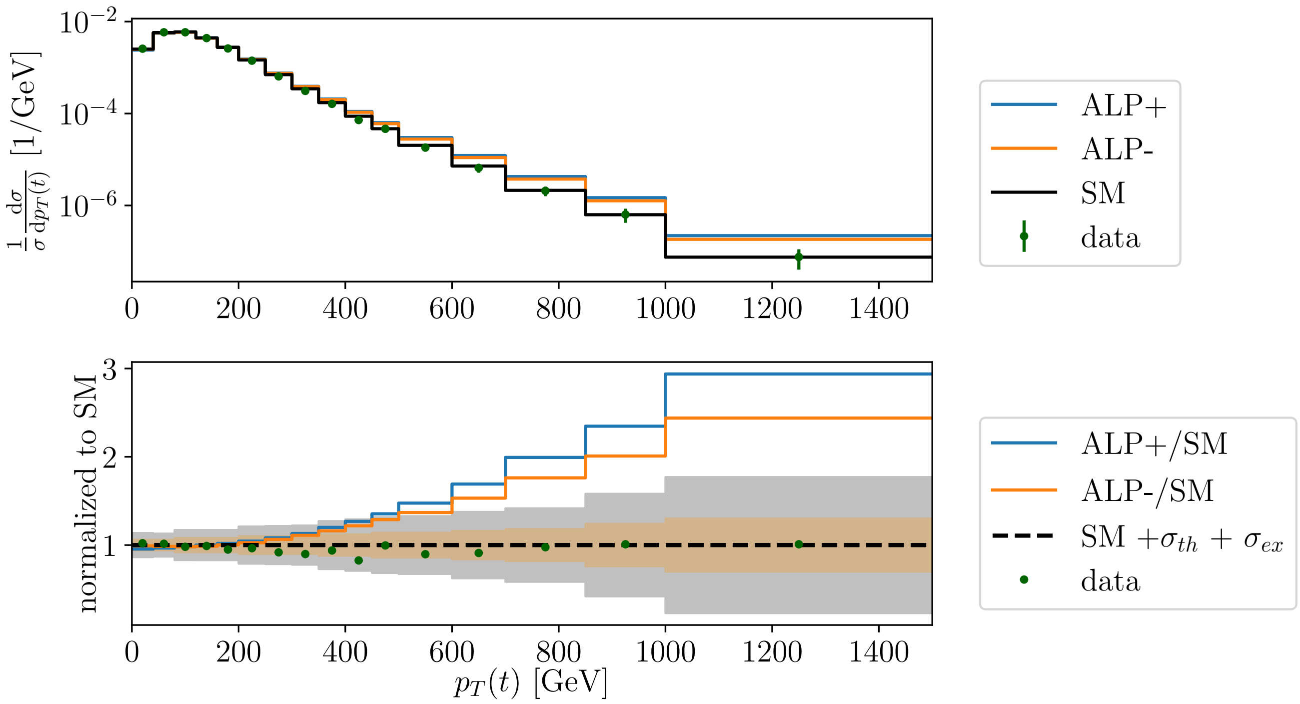

Figure 4.2: The upper diagram shows the normalized differential $t\bar{t}$ cross section as a function of top quark transverse momentum p_t for the ALP simulation with $(C_{ff}(\Lambda) \cdot C_{GG}(\Lambda))/f^2 = \pm 1$ TeV^{-2} corresponding to ALP+/- and the Standard Model NLO prediction together with the experimental data and the experimental uncertainties, both from CMS [25]. The lower diagram shows the differential cross section normalized to the Standard Model simulation as a function of p_t. The brown and silver area shows the theory and experimental uncertainties added in quadrature. The plot shows that the sensitivity of the ALP contribution is enhanced for large p_t values.

Figure 4.2 shows that the high p_t bins are more sensitive to the ALP contribution than the low p_t bins. By comparison of the scaling with s of the different contributions from Equations 4.1 it is seen that the ALP contribution is enhanced by s^2 and the interference contribution from the ALP model and the Standard Model is enhanced by s, which explains the enhancement in high energy distribution.

Since the $t\bar{t}$ production depends on both the ALP-fermion coupling $C_{tt}(\Lambda)$ and the ALP-gluon coupling $C_{GG}(\Lambda)$ it is only possible to constrain the product of the couplings, regardless of the observable. Figure 4.3 shows the bounds on $C_{GG}(\Lambda) \cdot C_{ff}(\Lambda)$. For $C_{ff}(\Lambda) \to 0$, $C_{GG}(\Lambda)$ can take arbitrarily large values and vice versa.

The numerical results are shown in Table 4.1. $\Delta\chi^2 = 5.9$ corresponds to a 2σ bound for a Gaussian distribution while $\Delta\chi^2 = 2.3$ corresponds to a 1σ bound. [17]

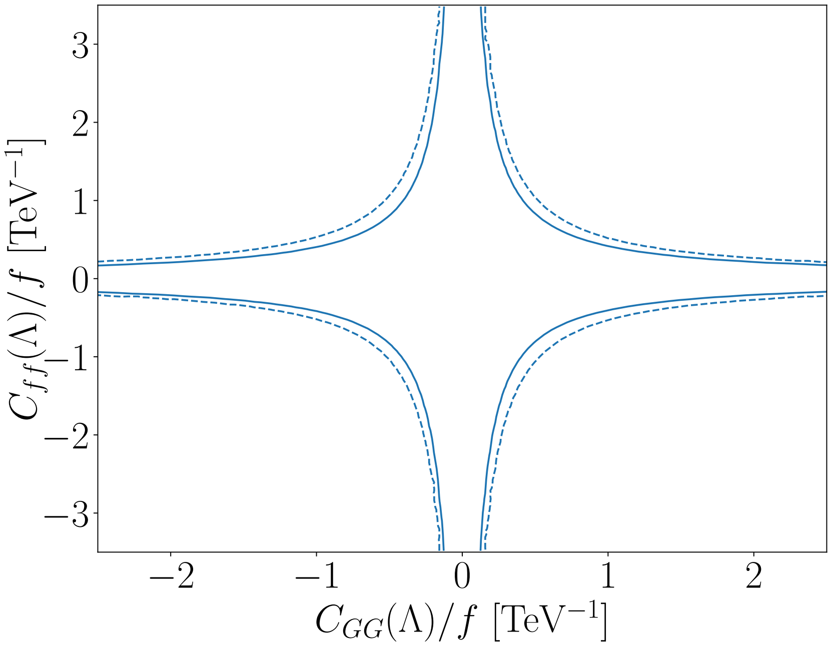

Figure 4.3: Bounds on $C_{GG}(\Lambda)$ and $C_{ff}(\Lambda)$. The dashed line shows the $\Delta\chi^2 = 5.9$ bound and the solid line shows the $\Delta\chi^2 = 2.3$ bound.

Table 4.1: Numerical values for the fit in Figure 4.3

	lower bounds		upper bounds	
$\Delta\chi^2$	2.3	5.9	2.3	5.9
$(C_{GG}(\Lambda) \cdot C_{ff}(\Lambda))/f^2$	-0.228 TeV^{-2}	-0.450 TeV^{-2}	0.225 TeV^{-2}	0.451 TeV^{-2}

4.2 ALPs in $t\bar{t}t\bar{t}$ production

Another way to test the ALPs couplings $C_{GG}(\Lambda)$ and $C_{tt}(\Lambda)$ is the measurement of $t\bar{t}t\bar{t}$ production cross section at ATLAS and CMS detector. As the cross section is small, there are no measurements of the p_t distributon yet which would also yield the difference in the coupling between the scalar and color-singlet ALP and the vector and color-octet gluon. In this chapter, we use the CMS measurements [26], [27] and the ATLAS measurements [28], [29] of the $t\bar{t}t\bar{t}$ production cross section as well as our ALP model simulations.

4.2.1 Theory

The ALP can contribute to the $pp \to t\bar{t}t\bar{t}$ production cross section through the $C_{GG}(m_t)$ and $C_{tt}(m_t)$ couplings. We assume flavor diagonality at the cutoff scale $\Lambda = 4\pi$ TeV. As the ALP-fermion coupling is expected to be Yukawa dependent (see Section 2.3) the ALP-top coupling is the dominating ALP-quark coupling. Figure 4.4 shows leading order Feynman diagrams for $t\bar{t}t\bar{t}$ production in pp collisions with a single ALP insertion, leading – with the possible interference with Standard Model diagrams – to amplitudes with ALP couplings of order two and four. Double ALP insertions as shown in Figure 4.5 are also possible, leading – with the possible interference with Standard Model diagrams – to amplitudes with ALP couplings of order four, six and eight. The large number of contributing ALP diagrams results in complicated calculations of predictions for differential cross sections.

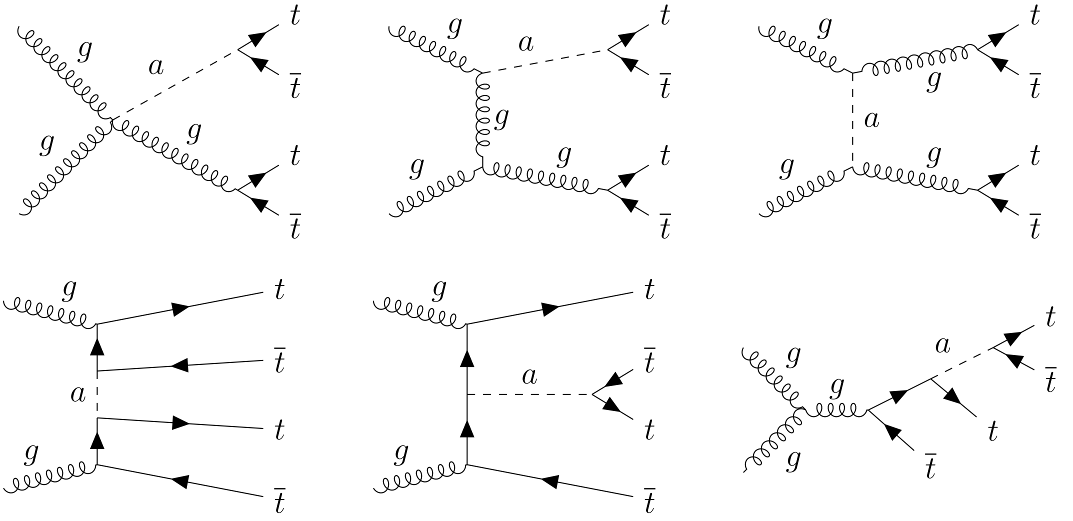

Figure 4.4: Example Feynman diagrams for the production of two top-antitop pairs including a single virtual ALP.

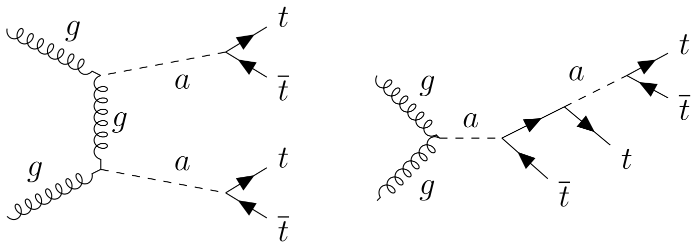

Figure 4.5: Example Feynman diagrams for the production of two top-antitop pairs including two virtual ALPs.

4.2.2 Methods

The setup was the same as the one in Section 4.1.2. Here, the additional challenge was that there were not only interference and squared terms, but also double insertions that potentially contribute significantly to the cross section, leading to amplitudes of ALP coupling of order four, six and eight. With various simulations at leading order (LO) in Madgraph5_aMC@NLO [21] with our FeynRules model [22] the individual contributions for the different combinations of the couplings could be found. This was done by setting one of the couplings to zero and setting the order of the ALP coupling in Madgraph5_aMC@NLO. The remaining contributions with linear combinations from both couplings where found numerically. For example amplitudes with ALP coupling order four there are contributions from terms proportional to $C_{GG}^4(\Lambda)$, $C_{GG}^3(\Lambda) \cdot C_{ff}(\Lambda)$, $C_{GG}^2(\Lambda) \cdot C_{ff}^2(\Lambda)$, $C_{GG}(\Lambda) \cdot C_{ff}^3(\Lambda)$, $C_{ff}^4(\Lambda)$. If we set one of the couplings to one and vary the other one it becomes a polynomial which can be solved numerically to obtain the different contributions.

We RG-evolved our predictions on the couplings $C_{GG}(m_t)$ and $C_{tt}(m_t)$ to obtain predictions on the couplings $C_{GG}(\Lambda)$ and $C_{ff}(\Lambda)$ with our implementation of the RG equations described in Section 3.2. For our `sfitter` [18] analysis we used four experimental measurements [26–29], which we assumed to be uncorrelated. The measurements show different results: The measured cross section results of the CMS measurements are 13^{+11}_{-9} fb [26] and $12.6^{+5.8}_{-5.2}$ fb [27] while the those of the ATLAS measurements are 24^{+7}_{-6} fb [28] and 26^{+17}_{-15} fb [27]. The NLO Standard Model prediction from Reference [30] was used. We assumed a generous theory uncertainty of 50 % for our LO simulations as Reference [30] calculated a 21 % uncertainty for their NLO predictions and to account for the differences between the experimental results.

4.2.3 Results

The $t\bar{t}t\bar{t}$ production cross section analysis is shown in Figure 4.6. Amplitudes with ALP couplings up to order eight were considered.

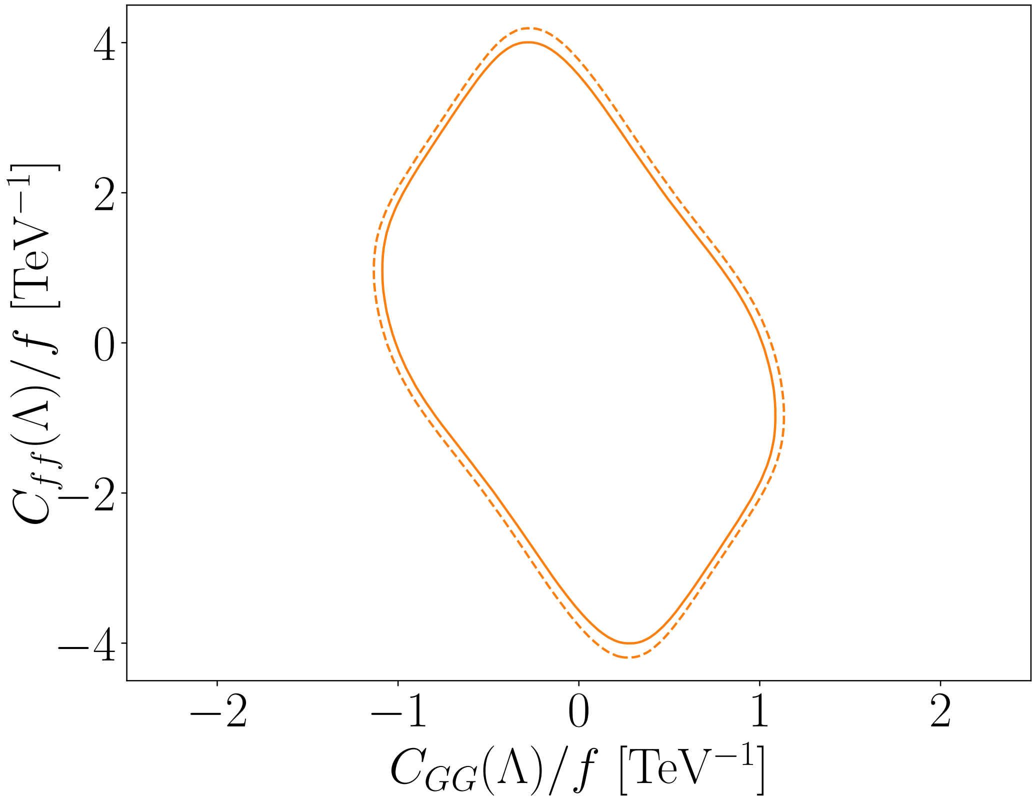

Figure 4.6: Bounds on $C_{GG}(\Lambda)$ and $C_{tt}(\Lambda)$. The dashed line shows the $\Delta\chi^2 = 5.9$ bound and the solid line shows the $\Delta\chi^2 = 2.3$ bound.

The numerical result is shown in Table 4.2. The $\Delta\chi^2 = 5.9$ bounds correspond to a 95 % CL bound for a Gaussian distribution, the $\Delta\chi^2 = 2.3$ bounds correspond to a 68 % CL bound for a Gaussian distribution.

Table 4.2: Numerical values for the fit in Figure 4.6.

	lower bounds		upper bounds	
$\Delta\chi^2$	2.3	5.9	2.3	5.9
$C_{GG}(\Lambda)/f$	-1.049 TeV^{-1}	-1.101 TeV^{-1}	1.049 TeV^{-1}	1.101 TeV^{-1}
$C_{ff}(\Lambda)/f$	-3.860 TeV^{-1}	-4.071 TeV^{-1}	3.860 TeV^{-1}	4.072 TeV^{-1}

4.3 ALPs in dijet production

Dijet angular distribution measurements provide a framework to constrain the ALP-gluon coupling $C_{GG}(\Lambda)$ and thus can resolve the ambiguity between $C_{tt}(\Lambda)$ and $C_{GG}(\Lambda)$ seen in the previous top analyses.

4.3.1 Theory

In the Standard Model dijets events are produced in scattering of quarks and gluons in proton-proton collisions, for example in the processes $gg \to gg$ and $qq \to qq$. [31] The angular distribution is expressed in terms of the quantity

$$\chi_{jj} = \exp |y_1 - y_2| \tag{4.4}$$

where y_1 and y_2 are the rapidities of the jets with the highest transverse momentum in the event. The rapidity is given by

$$y = \frac{E + p_z}{E - p_z} \tag{4.5}$$

with the energy of the jet E and the z-component of the momentum of the jet p_z, both in the center-of-mass frame of the proton-proton collision. [32]

The dominant dijet production processes with an ALP as a mediator are displayed in Figure 4.7.

Figure 4.7: Exemplary Feynman diagrams for the production of two jets mediated by a virtual ALP.

All other processes can be neglected because the ALP-quark coupling is heavily Yukawa suppressed except for the ALP-top coupling, which is loop suppressed as it only occurs in a top loop in the gluon gluon fusion process.

The ALP is a scalar particle; therefore, the angular distribution of the jets from a process with an ALP as a mediator differs from the SM process with vector bosons (mostly gluons, but photons and Z/W bosons are also possible) as a mediating particle. Thus, the dijet angular measurement is a way to probe the $C_{GG}(\Lambda)$ coupling individually. The ALP-gluon coupling $C_{GG}(\Lambda)$ is constant across the scales (see Section 2.3).

4.3.2 Methods

The tools used are the same as in section 4.1.2. The statistical concept is described in Section 3.1. The ALP UFO model file created with FeynRules [22] was implemented into Madgraph5_aMC@NLO [21]. The pdf set `nnpdf31_NLO_as_0118` [23] was used to avoid correlations in the top-sector. This pdf set is not based on top quark experiments so we can avoid correlations in the top-sector. The simulated data with the ALP model as well as experimental data and the Standard Model prediction [31] are used for the `sfitter` [18] analysis. To obtain the theory uncertainty we used the theory uncertainty of the NLO QCD predictions of Reference [31] and added a theoretic uncertainty of 5 % to account for the differences between these and our LO predictions. For the fit only the lowest mass bin with the jet invariant mass 2.4 TeV $< m_{jj} <$ 3.0 TeV was taken into account because it has the lowest uncertainties and is below the ALP cutoff scale $\Lambda = 4\,\pi$ TeV. Then every second χ_{jj} bin starting with bin number two was taken into account to circumvent the need to account for correlations between the bins. Since all the gauge couplings are constant across the scales there was no need to evolve the ALP-gluon coupling C_{GG} from the dijet scale to the cutoff scale Λ.

4.3.3 Results

Figure 4.8 shows the normalized differential cross section as a function of χ_{jj} for the Standard Model and the ALP simulation. The ALP χ_{jj} values differ significantly from the Standard Model, especially in the first bin.

Figure 4.9 shows the bound on $C_{GG}(\Lambda)$. The $\Delta\chi^2 = 2.3$ result (68 % CL for a Gaussian distribution) is $C_{GG}(\Lambda)/f = \pm\,0.646$ TeV^{-1} and the $\Delta\chi^2 = 5.9$ result (95 % CL for a Gaussian distribution) is $C_{GG}(\Lambda)/f = \pm\,0.662$ TeV^{-1}. The $\Delta\chi^2 = 2.3$ and $\Delta\chi^2 = 5.9$ are almost identical because the uncertainties are low.

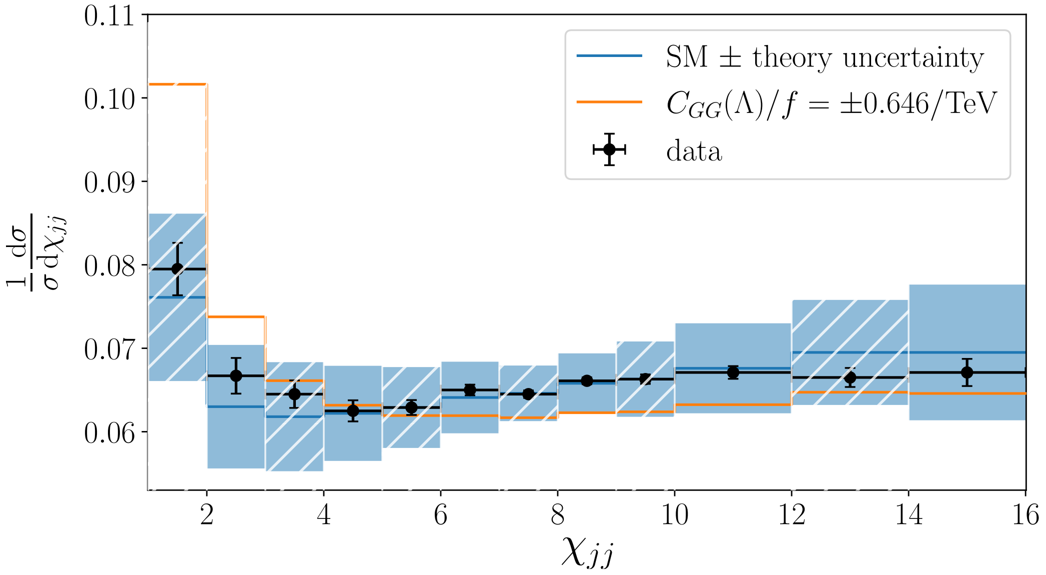

Figure 4.8: The normalized differential cross section as a function of χ_{jj} for the Standard Model simulation together with the theory uncertainty and the simulation with the ALP model with $C_{GG}(\Lambda) = \pm 0.646$ ($\Delta\chi^2 = 2.3$ bound). We only used the hatched bins for our analysis.

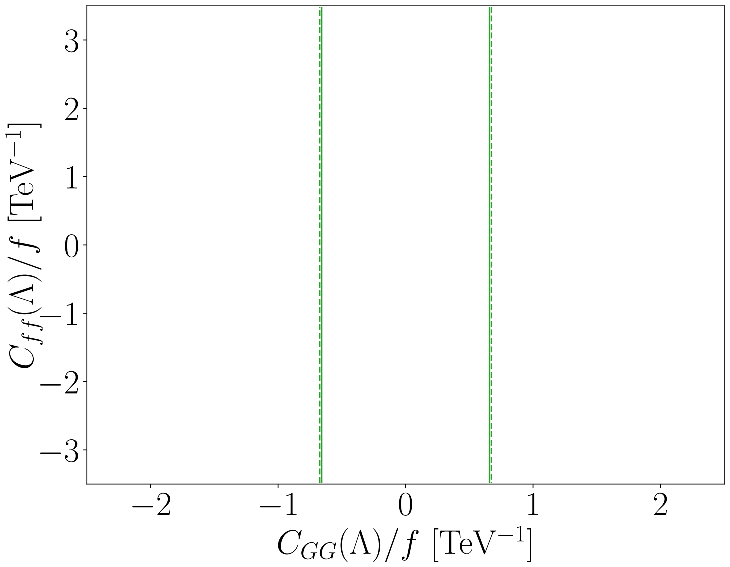

Figure 4.9: Bounds on $C_{GG}(\Lambda)$. The solid line corresponds to the $\Delta\chi^2 = 2.3$ result (68 % CL for a Gaussian distribution) and the dashed line to the $\Delta\chi^2 = 5.9$ result (95 % CL for a Gaussian distribution).

4.4 ALPs in flavor observables

The renormalization group (RG) equations can be used to evolve the couplings across the scales and therefore enable us to compare different measurements at different scales with each other. Flavor observables like the $b \to s$ transition are highly sensitive to new physics and can be measured in B meson decays in B-factories. [33] In this chapter, $B \to KX(\to l^+l^-)$ searches from LHCb [34] and searches from BaBar with missing energy $B \to K\not{E}$ [35] have been interpreted in the ALP framework to obtain constrains on the ALP-fermion coupling $C_{ff}(\Lambda)$ and the ALP-W boson coupling $C_{WW}(\Lambda)$. This combination of invisible and displaced searches provides another strong constraint on the ALP couplings.

4.4.1 Theory

In B meson decays, the ALP is produced through the effective coupling C_{sb}. At one-loop level it is given by:

$$C_{sb}(m_a) = 7.7910 \cdot 10^{-4} \cdot C_{ff}(\Lambda) - 1.19 \cdot 10^{-6} \cdot C_{WW}(\Lambda) \tag{4.6}$$

which can be calculated with the use of our implementation of the renormalization group equations described in Section 3.2. We assume flavor diagonality at the cutoff $\Lambda = 4\pi f$ with the ALP decay constant $f = 1$ TeV. For the analysis of flavor observables, at the cutoff scale all couplings except the ALP-fermion coupling $C_{ff}(\Lambda)$ and ALP-W boson coupling $C_{WW}(\Lambda)$ are set to zero. $C_{WW}(\Lambda)$ is constant across the scales as it does not run. The ALP Lagrangian and the running of the couplings down to the flavor scale is described in section 2.3. The on-shell production rate is given by:

$$\Gamma_{B\to Ka} = \frac{C_{sb}^2(m_a)}{4\Lambda^2}\pi\, f_0^2(m_a^2)\, m_B \left(1 - \frac{m_K^2}{m_B^2}\right)^2 \lambda^{1/2}\left(m_B^2, m_K^2, m_a^2\right) \tag{4.7}$$

with the kinematic function $\lambda^{1/2}\left(m_B^2, m_K^2, m_a^2\right) = a^2 + b^2 + c^2 - 2\,(ab + ac + bc)$. [36]. The scalar form factor $f_0^2(m_a^2)$ is implemented from Reference [37].

For small lifetimes the ALP will decay in the detector, e.g. into photons or muons. For longer lifetimes the ALP leaves a trace of missing energy in the detector as a long-lived particle. The ALP production and the decay into leptons is shown in Figure 4.10. In the Standard Model, a $B \to K\mu\mu$ decay is also possible, e.g. through an intermediate Z boson or a photon, which couples to the top quark and then decays into two leptons.

At a hypothetical ALP mass $m_a = 0.3$ GeV ALPs mostly decay into muons as the

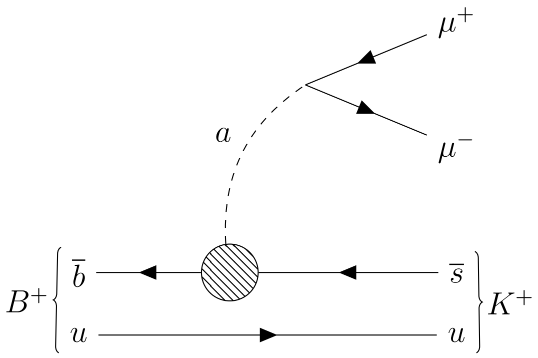

a) effective coupling C_{sb}

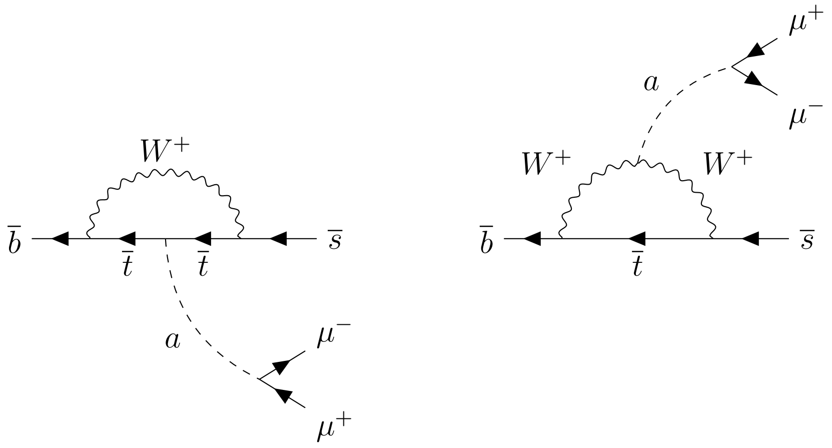

b) $C_{ff}(m_b)$ coupling (left) and $C_{WW}(m_b)$ coupling (right) that contribute to the effective coupling C_{sb}

Figure 4.10: Feynman diagrams for the decay $B \to Ka, a \to \mu^+\mu^-$.

decay into electrons is suppressed due to the lighter electron mass: [36]

$$\Gamma_{a\to l\bar{l}} = 2\,\pi\,|C_{ff}(m_a)|^2\,\frac{m_a\,m_l^2}{\Lambda^2}\sqrt{1-\frac{4m_l^2}{m_a^2}} \tag{4.8}$$

For small $C_{ff}(\Lambda)$ ALPs mostly decay into photons with a partial width given by [36]

$$\Gamma_{a\to\gamma\gamma} = \frac{\alpha^2}{4\pi}\,|C_{\gamma\gamma}^{\text{eff}} m_a|^2 \frac{m_a^3}{\Lambda^2} \tag{4.9}$$

and effective photon coupling (for $C_{BB} = 0$) [36]

$$C_{\gamma\gamma}^{\text{eff}}(m_a) \approx C_{WW} + \mathcal{O}\left(\frac{\alpha}{4\pi}C_{ff}\right). \tag{4.10}$$

For an ALP mass of $m_a = 0.3$ GeV the decay total width is given by:

$$\Gamma_a = \Gamma_{a\to\gamma\gamma} + \Gamma_{a\to\mu^+\mu^-} \tag{4.11}$$

The lifetime of the ALP can be determined as follows:

$$\tau_a = \frac{1}{\Gamma_a} \tag{4.12}$$

4.4.2 Methods

The number of $B^+ \to K^+X, X \to \mu^+\mu^-$ events increases in the ALP model with respect to the Standard Model prediction, thus measurements can provide constraints to the ALP couplings $C_{ff}(\Lambda)$ and $C_{WW}(\Lambda)$ for the ALP mass $m_a < m_B - m_K$. We analysed constraints on the couplings $C_{ff}(\Lambda)$ and $C_{WW}(\Lambda)$ for a fixed ALP mass $m_a = 0.3$ GeV. This mass was chosen because ALP decays to pions are not yet possible but decays to muons are. This constellation provides a high sensitivity of the experiments. For the analysis the LHCb data in Figure 4 of Reference [34] provides us with 95 % CL exclusion limits for the $B^+ \to K^+X, X \to \mu^+\mu^-$ decay as a function of the branching ratio, the lifetime and the mass of the particle X. We sample through the couplings $C_{ff}(\Lambda)$ and $C_{WW}(\Lambda)$ and calculate the branching ratio and lifetime for each individual data point to compare it to the measurement. For this step we make use of our implementation of the renormalization group evolution equations from Reference [12] at one loop level as it is described in Section 3.2.

Another bound is provided by searches for missing energy which can be reinterpreted as a long-lived ALP that does not decay in the detector. As it leaves a signature of missing energy, the number of events is increased in the ALP model compared to the Standard Model. The analysis with data from the BaBar experiment from Reference [36] is extended for an analysis for two couplings. Branching ratio and lifetime are calculated in the same way as before and in an analogous manner compared to the 95 % CL values of the experimental data, here from the BaBar measurement [35].

4.4.3 Results

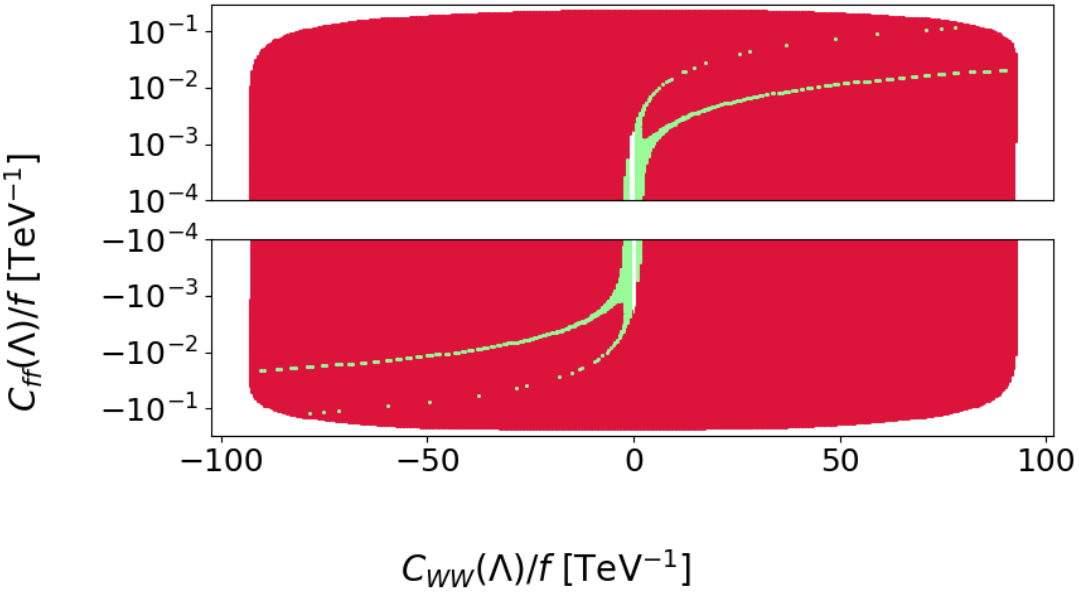

a) Overall view on bounds from LHCb on $C_{WW}(\Lambda)$ and $C_{ff}(\Lambda)$.

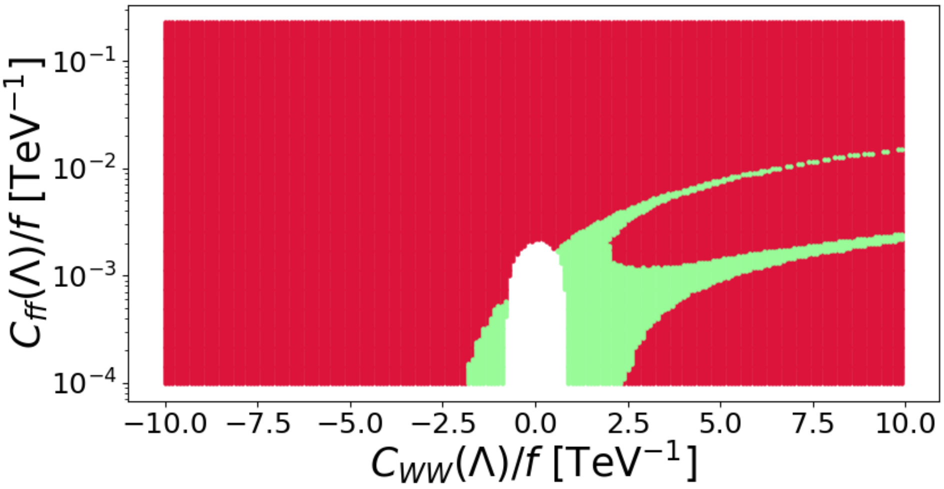

b) Zoom plot on bounds from LHCb on $C_{WW}(\Lambda)$ and $C_{ff}(\Lambda)$.

Figure 4.11: Bounds from LHCb on $C_{WW}(\Lambda)$ and $C_{ff}(\Lambda)$, the latter is shown on a logarithmic scale for both positive and negative values (only positive values in the zoom plot). The red area shows the excluded region while the green area is allowed within the current measurements. The white region in the middle and on the sides cannot be excluded because the decays are too long-lived/too prompt.

Figure 4.11a) shows the excluded region from the interpretation of the muon pair detection by the LHCb measurement. A zoom plot in Figure 4.11b) shows the white area, where the couplings cannot be excluded due to the lifetime, and the two blind directions, where the ALP couplings can not be excluded, in detail. The upper blind direction is due to the interference in the production ($C_{sb} = 0$). The second blind direction comes from the ALP decay. For small $C_{ff}(\Lambda)$ and large $C_{WW}(\Lambda)$ couplings the branching ratio for $a \to \mu\mu$ has a minimum at $C_{ff}(\Lambda) \neq 0$ as it is shown in Figure 4.12.

The squared ALP-lepton coupling at the ALP mass scale, which is used in the calculation of the decay width in Equation 4.8, also contains loop-suppressed C_{WW} contributions:

$$C_{ll}^2(m_a) = \mathcal{O}\left(C_{ff}^2(\Lambda)\right) - \mathcal{O}\left(2\,C_{ff}(\Lambda)\,C_{WW}(\Lambda)\frac{\alpha^2}{16\pi^2}\right) + \mathcal{O}\left(\left(\frac{\alpha^2}{16\pi^2}\right)^2 C_{WW}^2(\Lambda)\right) \tag{4.13}$$

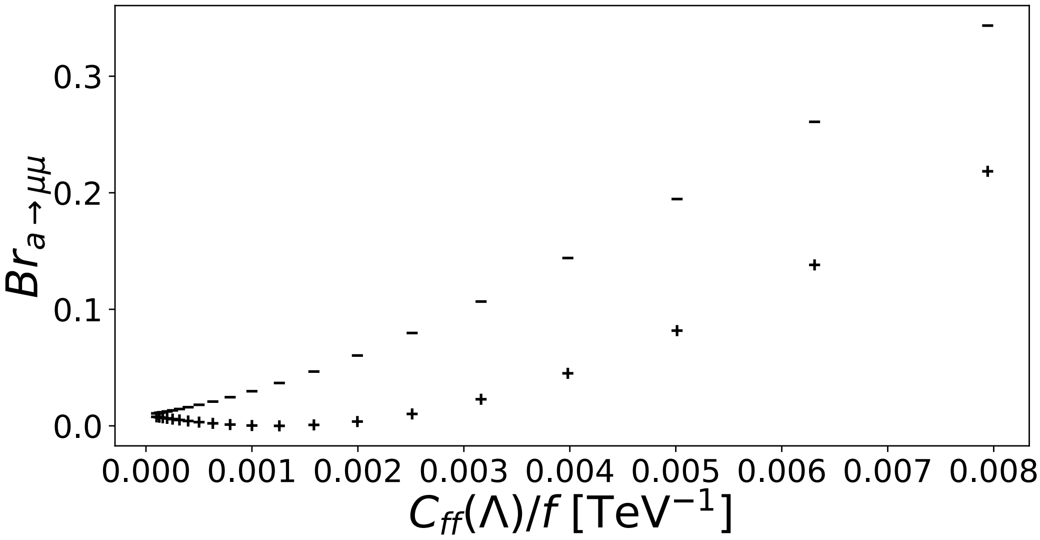

Figure 4.12: Predicted branching ratio $Br_{a\to\mu\mu}$ as a function of $C_{ff}(\Lambda)$ for $C_{WW} = 5$ (+) and $C_{WW} = -5$ (-).

Figure 4.12 illustrates the case where $C_{ff}(\Lambda)$ approaches zero for a fixed positive $C_{WW}(\Lambda)$ coupling. Then the decay width into photons is constant. Therefore, the branching ratio only depends on the decay width into muons $\Gamma_{\mu\mu}$. As $\Gamma_{\mu\mu} \ll \Gamma_{\gamma\gamma}$, the branching ratio is approximately proportional to the coupling $Br_{a\to\mu\mu} \propto (C_{ll}(m_a))^2$ (see Equation 4.13). The branching ratio thus follows a parabolic curve, whose minimum is shifted away from $C_{ff}(\Lambda) = 0$ by the interference term $-\mathcal{O}\left(2\, C_{ff}(\Lambda)\, C_{WW}(\Lambda) \frac{\alpha^2}{16\pi^2}\right)$. For positive (negative) $C_{WW}(\Lambda)$, the minimum is therefore shifted to $C_{ff}(\Lambda) > 0$ ($C_{ff}(\Lambda) < 0$) by a value proportional to $C_{WW}(\Lambda)$. The minimum of the branching ratio $Br_{a\to\mu\mu}$ is below the exclusion limit of the LHCb measurement thus resulting in a blind direction. Figure 4.13 shows the product of the production and decay branching ratios ($Br_{B\to Ka} \cdot Br_{a\to\mu\mu}$) and illustrates the two blind directions.

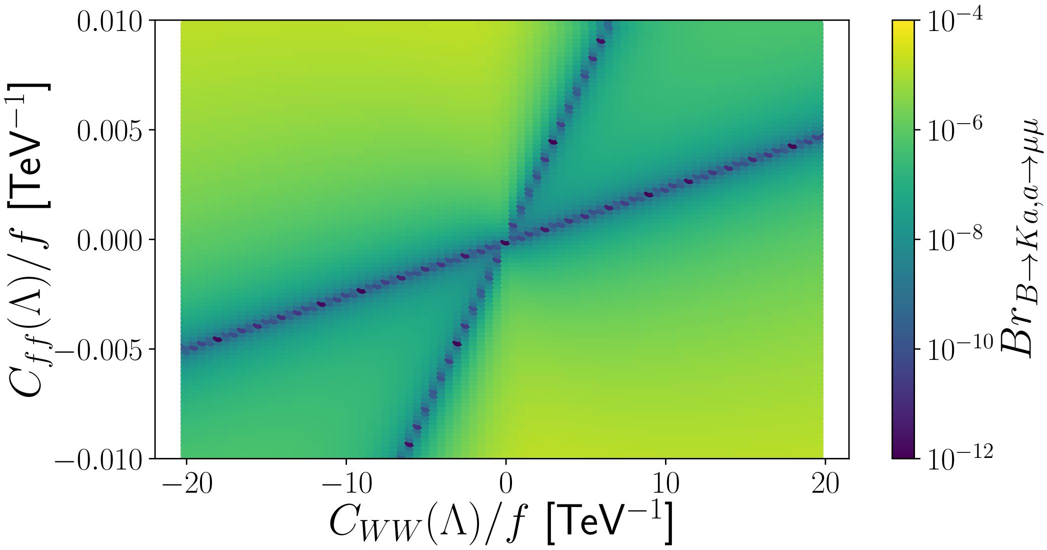

Figure 4.13: ALP production and decay into muons branching ratio as a function of the couplings $C_{ff}(\Lambda)$ and $C_{WW}(\Lambda)$.

Figure 4.14 shows the combined bound from both the LHCb and BaBar measurement. The LHCb contribution to this diagram can be identified by the blind directions as thin lines and the excluded ellipse around it. The BaBar bound leaves a band where the couplings cannot be excluded by the BaBar measurement with two ellipses in the middle where the experiment is sensitive.

Because the BaBar search looks for missing energy, the detection depends on an interplay of lifetime and production rate. The lifetime needs to be long enough that the ALPs decay behind the detector and leave a trace of missing energy. For a long lifetime, the ALP couplings needs to be small. On the other hand the $C_{ff}(\Lambda)$ coupling needs to be sufficiently large to obtain a high production rate. This results

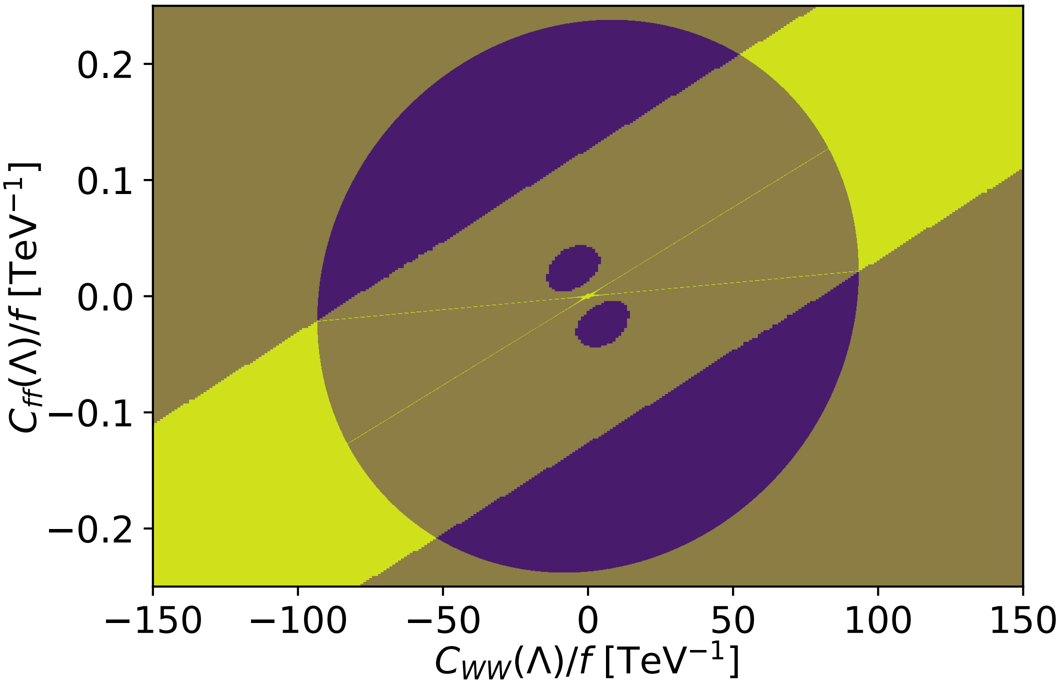

Figure 4.14: Combined bounds from BaBar and LHCb on $C_{WW}(\Lambda)$ and $C_{ff}(\Lambda)$. The yellow area can not be excluded with the measurements, the purple area is excluded by both measurements and the brown area is excluded by one measurement.

in the two ellipses where the couplings can be excluded. Starting at both $C_{ff}(\Lambda) = C_{WW}(\Lambda) = 0$ the production rate is too small to set a bound. With increasing $C_{ff}(\Lambda)$ even though the rate is small the lifetime is at maximum so almost all ALPs decay outside the detector and there are enough ALPs leaving a missing energy signature to set a bound which leads to the purple ellipses in Figure 4.14 where the couplings can be excluded. With increasing $C_{ff}(\Lambda)$ coupling the lifetime becomes smaller and reaches a point where the interplay of production rate and lifetime is too small to set a bound. With further increasing $C_{ff}(\Lambda)$ coupling the amount of ALPs leaving a missing energy signature becomes large enough again to set a bound. This is the geometric bound as approximately all ALPs decay inside the detector but because of the geometric detector coverage some ALPs still leave a trace of missing energy. And since the production rate is large there are enough predicted missing energy events to set this bound.

5 Summary and Outlook

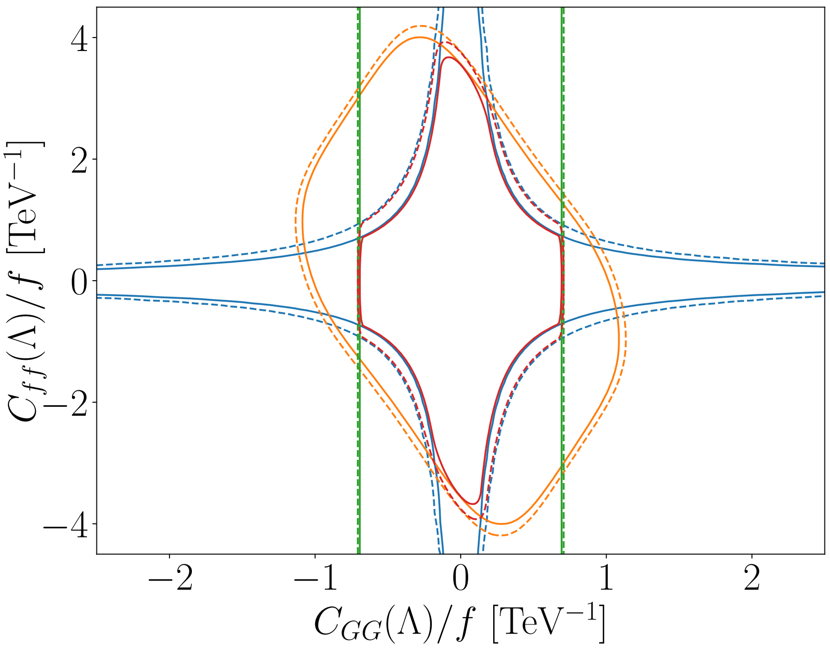

Figure 5.1: Combined fit (red) for the ALP couplings $C_{tt}(\Lambda)$ and $C_{GG}(\Lambda)$. The plot combines the results from $t\bar{t}$ production (blue), $t\bar{t}t\bar{t}$ production (orange) and dijet angular distribution (green). The dashed lines show the $\Delta\chi^2 = 5.9$ bounds and the solid lines show the $\Delta\chi^2 = 2.3$ bounds.

The aim of this work was to combine different ALP senstive observables to resolve the coupling space of $C_{ff}(\Lambda)$, $C_{GG}(\Lambda)$ and $C_{WW}(\Lambda)$. The results of the high energy analyses are combined in one `sfitter` [18] fit (Figure 5.1). The numerical results are shown in Table 5.1. We work in a flavor aligned model and all other couplings are set to zero at the ALP cutoff scale Λ. As expected the Standard Model which is equivalent to setting $C_{GG}(\Lambda) = C_{ff}(\Lambda) = 0$ is not excluded.

The $t\bar{t}$ production analysis and the dijet angular distribution analysis showed that the angular distribution of an ALP differs compared to a gluon because it is scalar and color-singlet. The $t\bar{t}$ analysis also showed that the ALP contribution is enhanced for high energy due to its scaling with s (interference term ALP and Standard Model) and s^2 (ALP squared term).

Table 5.1: Numerical values for the fit in Figure 5.1.

	lower bounds		upper bounds	
$\Delta\chi^2$	2.3	5.9	2.3	5.9
$C_{GG}(\Lambda)/f$	-0.680 TeV^{-1}	-0.695 TeV^{-1}	0.681 TeV^{-1}	0.695 TeV^{-1}
$C_{ff}(\Lambda)/f$	-3.485 TeV^{-1}	-3.775 TeV^{-1}	3.485 TeV^{-1}	3.775 TeV^{-1}

The $t\bar{t}t\bar{t}$ production analysis was challenging because higher order terms contributed significantly and it was limited by the experimental data because there are only measurements of the cross section yet. However, the analysis resolved the blind directions of $C_{tt}(\Lambda)\cdot C_{GG}(\Lambda)$. Future measurements with observables like the tranverse momentum p_t or the rapidity y could yield stronger bounds on the ALP coupling than the $t\bar{t}$ production analysis.

In the flavor sector we interpreted searches $B \to KX(\to l^+l^-)$ from LHCb and searches for missing energy from BaBar $B \to K\not{E}$ to confine the ALP couplings $C_{ff}(\Lambda)$ and $C_{WW}(\Lambda)$. The results in Figure 4.11a) and 4.14 show the excluded areas and the blind directions. The flavor observables have a strong sensitivity to $C_{ff}(\Lambda)$. It would have been even stronger if we did not choose flavor diagonal couplings at the cutoff scale. The ALP production coupling C_{sb} is an off-diagonal entry and thus its value at the low scale μ_f only arises from matching contributions. The experimental data was only given as 95 % CL exclusion limits which did not allow us to use it for a fit. Our flavor analysis has weaker sensitivity to the ALP-W boson coupling $C_{WW}(\Lambda)$. Additional observables like the diboson cross section (analysis in Reference [38]) would provide an additional bound on $C_{WW}(\Lambda)$.

Our analysis is a first step towards a global fit. A global fit with a more general flavor structure, the ALP mass m_a as a free parameter and bounds on $C_{BB}(\Lambda)$ is left to future work. While there are no clear hints for a presence of ALPs in the evaluated data, the ALP model remains possible within the bounds we found. The ALP model might then solve current open questions like the strong CP problem and the search for dark matter.

Part I

Appendix

A Feynman rules

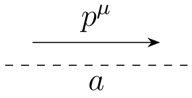

$$\frac{-\,i}{m^2+p^2}$$

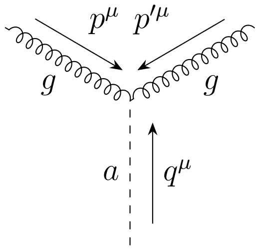

$$i\,\frac{C_{GG}}{f}\,\frac{\alpha_s}{\pi}\,\delta_{ab}\,p_\nu\,p'_\rho\,\epsilon^{\mu\nu\rho\sigma}$$

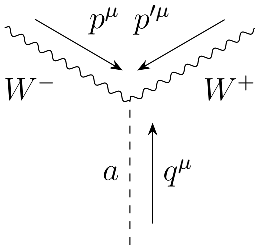

$$i\,\frac{C_{WW}}{f}\,\frac{\alpha_2}{\pi}\,p_\nu\,p'_\rho\,\epsilon^{\mu\nu\rho\sigma}$$

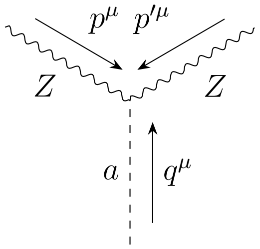

$$i\,\frac{C_{WW}\cos^2\theta\,\alpha_2+C_{BB}\sin^2\theta\,\alpha_1}{f\;\pi}\,p_\nu\,p'_\rho\,\epsilon^{\mu\nu\rho\sigma}$$

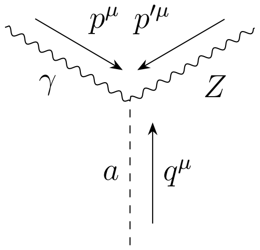

$$i\,\left(C_{WW}\,\alpha_2-C_{BB}\,\alpha_1\right)\frac{2\sin\theta\cos\theta}{f\;\pi}\,p_\nu\,p'_\rho\,\epsilon^{\mu\nu\rho\sigma}$$

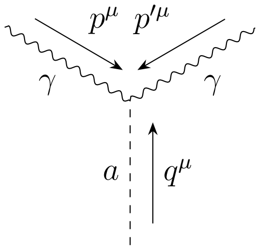

$$i\,\frac{C_{WW}\sin^2\theta\,\alpha_2 + C_{BB}\cos^2\theta\,\alpha_1}{f\;\pi}\,p_\nu\,p'_\rho\,\epsilon^{\mu\nu\rho\sigma}$$

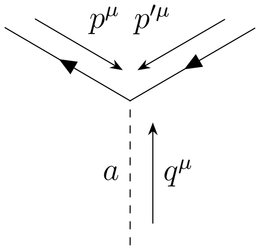

$$\not{q}\,\frac{1}{f}\,[(C_F)_{ij}P_R + (C_f)_{ij}P_L]$$

B Lists

B.1 List of Figures

B.2 List of Tables

C Bibliography

[1] Hyun Min Lee. “Lectures on physics beyond the Standard Model”. In: *Journal of the Korean Physical Society* (May 2021). ISSN: 1976-8524. DOI: `10.1007/s40042-021-00188-x`. URL: `http://dx.doi.org/10.1007/s40042-021-00188-x`.

[2] R. D. Peccei and Helen R. Quinn. “CP Conservation in the Presence of Pseudoparticles”. In: *Phys. Rev. Lett.* 38 (25 June 1977), pp. 1440–1443. DOI: `10.1103/PhysRevLett.38.1440`. URL: `https://link.aps.org/doi/10.1103/PhysRevLett.38.1440`.

[3] R. D. Peccei and Helen R. Quinn. “Constraints imposed by CP conservation in the presence of pseudoparticles”. In: *Phys. Rev. D* 16 (6 Sept. 1977), pp. 1791–1797. DOI: `10.1103/PhysRevD.16.1791`. URL: `https://link.aps.org/doi/10.1103/PhysRevD.16.1791`.

[4] Steven Weinberg. “A New Light Boson?” In: *Phys. Rev. Lett.* 40 (4 Jan. 1978), pp. 223–226. DOI: `10.1103/PhysRevLett.40.223`. URL: `https://link.aps.org/doi/10.1103/PhysRevLett.40.223`.

[5] F. Wilczek. “Problem of Strong P and T Invariance in the Presence of Instantons”. In: *Phys. Rev. Lett.* 40 (5 Jan. 1978), pp. 279–282. DOI: `10.1103/PhysRevLett.40.279`. URL: `https://link.aps.org/doi/10.1103/PhysRevLett.40.279`.

[6] Eduard Massó, Francesc Rota, and Gabriel Zsembinszki. “Planck-scale effects on global symmetries: Cosmology of pseudo-Goldstone bosons”. In: *Physical Review D* 70.11 (Dec. 2004). ISSN: 1550-2368. DOI: `10.1103/physrevd.70.115009`. URL: `http://dx.doi.org/10.1103/PhysRevD.70.115009`.

[7] Paola Arias et al. “WISPy cold dark matter”. In: *Journal of Cosmology and Astroparticle Physics* 2012.06 (June 2012), p. 013. ISSN: 1475-7516. DOI: `10.1088/1475-7516/2012/06/013`. URL: `http://dx.doi.org/10.1088/1475-7516/2012/06/013`.

[8] Marat Freytsis and Zoltan Ligeti. “Dark matter models with uniquely spin-dependent detection possibilities”. In: *Physical Review D* 83.11 (June 2011). ISSN: 1550-2368. DOI: `10.1103/physrevd.83.115009`. URL: `http://dx.doi.org/10.1103/PhysRevD.83.115009`.

[9] Keith R. Dienes et al. “Overcoming velocity suppression in dark-matter direct-detection experiments”. In: *Physical Review D* 90.1 (July 2014). ISSN: 1550-2368. DOI: `10.1103/physrevd.90.015012`. URL: `http://dx.doi.org/10.1103/PhysRevD.90.015012`.

[10] Joerg Jaeckel and Michael Spannowsky. “Probing MeV to 90 GeV axion-like particles with LEP and LHC”. In: *Physics Letters B* 753 (Feb. 2016), pp. 482–487. ISSN: 0370-2693. DOI: `10.1016/j.physletb.2015.12.037`. URL: `http://dx.doi.org/10.1016/j.physletb.2015.12.037`.

[11] Howard Georgi, David B. Kaplan, and Lisa Randall. “Manifesting the invisible axion at low energies”. In: *Physics Letters B* 169.1 (1986), pp. 73–78. ISSN: 0370-2693. DOI: `https://doi.org/10.1016/0370-2693(86)90688-X`. URL: `https://www.sciencedirect.com/science/article/pii/037026938690688X`.

[12] Martin Bauer et al. “The low-energy effective theory of axions and ALPs”. In: *Journal of High Energy Physics* 2021.4 (Apr. 2021). ISSN: 1029-8479. DOI: `10.1007/jhep04(2021)063`. URL: `http://dx.doi.org/10.1007/JHEP04(2021)063`.

[13] I. Brivio et al. “ALPs effective field theory and collider signatures”. In: *The European Physical Journal C* 77.8 (Aug. 2017). ISSN: 1434-6052. DOI: `10.1140/epjc/s10052-017-5111-3`. URL: `http://dx.doi.org/10.1140/epjc/s10052-017-5111-3`.

[14] Michael Edward Peskin and Daniel V. Schroeder. *An Introduction to Quantum Field Theory*. Reading, USA: Addison-Wesley (1995) 842 p. Westview Press, 1995.

[15] Anja Butter. “Global Fits for New Physics at the LHC and Beyond”. PhD thesis. U. Heidelberg (main), 2017. DOI: `10.11588/heidok.00023710`.

[16] S. S. Wilks. “The Large-Sample Distribution of the Likelihood Ratio for Testing Composite Hypotheses”. In: *The Annals of Mathematical Statistics* 9.1 (1938), pp. 60–62. DOI: `10.1214/aoms/1177732360`. URL: `https://doi.org/10.1214/aoms/1177732360`.

[17] P.A. Zyla et al. “Review of Particle Physics”. In: *PTEP* 2020.8 (2020), p. 083C01. DOI: `10.1093/ptep/ptaa104`.

[18] Remi Lafaye, Tilman Plehn, and Dirk Zerwas. *SFITTER: SUSY parameter analysis at LHC and LC*. Apr. 2004. arXiv: `hep-ph/0404282 [hep-ph]`.

[19] Sebastian Bruggisser et al. “The flavor of UV physics”. In: *Journal of High Energy Physics* 2021.5 (May 2021). ISSN: 1029-8479. DOI: `10.1007/jhep05(2021)257`. URL: `http://dx.doi.org/10.1007/JHEP05(2021)257`.

[20] Ilaria Brivio et al. “O new physics, where art thou? A global search in the top sector”. In: *Journal of High Energy Physics* 2020.2 (Feb. 2020). ISSN: 1029-8479. DOI: `10.1007/jhep02(2020)131`. URL: `http://dx.doi.org/10.1007/JHEP02(2020)131`.

[21] J. Alwall et al. “The automated computation of tree-level and next-to-leading order differential cross sections, and their matching to parton shower simulations”. In: *Journal of High Energy Physics* 2014.7 (July 2014). ISSN: 1029-8479. DOI: `10.1007/jhep07(2014)079`. URL: `http://dx.doi.org/10.1007/JHEP07(2014)079`.

[22] Adam Alloul et al. “FeynRules 2.0 – A complete toolbox for tree-level phenomenology”. In: *Computer Physics Communications* 185.8 (Aug. 2014), pp. 2250–2300. ISSN: 0010-4655. DOI: `10.1016/j.cpc.2014.04.012`. URL: `http://dx.doi.org/10.1016/j.cpc.2014.04.012`.

[23] Richard D. Ball et al. “Parton distributions from high-precision collider data”. In: *The European Physical Journal C* 77.10 (Oct. 2017). ISSN: 1434-6052. DOI: `10.1140/epjc/s10052-017-5199-5`. URL: `http://dx.doi.org/10.1140/epjc/s10052-017-5199-5`.

[24] *Measurement of the $t\bar{t}$ production cross-section and lepton differential distributions in $e\mu$ dilepton events from pp collisions at $\sqrt{s} = 13$ TeV with the ATLAS detector*. Tech. rep. All figures including auxiliary figures are available at https://atlas.web.cern.ch/Atlas/GROUPS/PHYSICS/CONFNOTES/ATLAS-CONF-2019-041. Geneva: CERN, Aug. 2019. URL: `https://cds.cern.ch/record/2686255`.

[25] *Measurement of differential $t\bar{t}$ production cross sections in the full kinematic range using lepton+jets events from pp collisions at $\sqrt{s} = 13$* TeV. Tech. rep. Geneva: CERN, 2021. URL: `http://cds.cern.ch/record/2759302`.

[26] A. M. Sirunyan et al. “Search for the production of four top quarks in the single-lepton and opposite-sign dilepton final states in proton-proton collisions at $\sqrt{s} = 13$ TeV”. In: *Journal of High Energy Physics* 2019.11 (Nov. 2019). ISSN: 1029-8479. DOI: `10.1007/jhep11(2019)082`. URL: `http://dx.doi.org/10.1007/JHEP11(2019)082`.

[27] A. M. Sirunyan et al. “Search for production of four top quarks in final states with same-sign or multiple leptons in proton–proton collisions at $\sqrt{s} = 13$ TeV”. In: *The European Physical Journal C* 80.2 (Jan. 2020). ISSN: 1434-6052. DOI: `10.1140/epjc/s10052-019-7593-7`. URL: `http://dx.doi.org/10.1140/epjc/s10052-019-7593-7`.

[28] Georges Aad et al. “Evidence for $t\bar{t}t\bar{t}$ production in the multilepton final state in proton–proton collisions at $\sqrt{s} = 13$ TeV with the ATLAS detector”. In: *Eur. Phys. J. C* 80.11 (2020), p. 1085. DOI: `10.1140/epjc/s10052-020-08509-3`. arXiv: `2007.14858 [hep-ex]`.

[29] Georges Aad et al. "Measurement of the $t\bar{t}t\bar{t}$ production cross section in pp collisions at $\sqrt{s} = 13$ TeV with the ATLAS detector". In: *JHEP* 11 (2021), p. 118. DOI: `10.1007/JHEP11(2021)118`. arXiv: `2106.11683 [hep-ex]`.

[30] Rikkert Frederix, Davide Pagani, and Marco Zaro. "Large NLO corrections in $t\bar{t}W^{\pm}$ and $t\bar{t}t\bar{t}$ hadroproduction from supposedly subleading EW contributions". In: *Journal of High Energy Physics* 2018.2 (Feb. 2018). ISSN: 1029-8479. DOI: `10.1007/jhep02(2018)031`. URL: `http://dx.doi.org/10.1007/JHEP02(2018)031`.

[31] A. M. Sirunyan et al. "Search for new physics in dijet angular distributions using proton-proton collisions at $\sqrt{s} = 13$ TeV and constraints on dark matter and other models". In: *The European Physical Journal C* 78.9 (Sept. 2018). ISSN: 1434-6052. DOI: `10.1140/epjc/s10052-018-6242-x`. URL: `http://dx.doi.org/10.1140/epjc/s10052-018-6242-x`.

[32] G. Aad et al. *ATLAS search for new phenomena in dijet mass and angular distributions using pp collisions at* $\sqrt{s} = 7$ TeV. Jan. 2013. DOI: `10.1007/jhep01(2013)029`. URL: `http://dx.doi.org/10.1007/JHEP01(2013)029`.

[33] E Kou et al. "The Belle II Physics Book". In: *Progress of Theoretical and Experimental Physics* 2019.12 (Dec. 2019). ISSN: 2050-3911. DOI: `10.1093/ptep/ptz106`. URL: `http://dx.doi.org/10.1093/ptep/ptz106`.

[34] R. Aaij et al. "Search for long-lived scalar particles in $B^+ \to K^+\chi(\mu^+\mu^-)$ decays". In: *Physical Review D* 95.7 (Apr. 2017). ISSN: 2470-0029. DOI: `10.1103/physrevd.95.071101`. URL: `http://dx.doi.org/10.1103/PhysRevD.95.071101`.

[35] J. P. Lees et al. "Search for $B \to K^{(*)}\nu\overline{\nu}$ and invisible quarkonium decays". In: *Physical Review D* 87.11 (June 2013). ISSN: 1550-2368. DOI: `10.1103/physrevd.87.112005`. URL: `http://dx.doi.org/10.1103/PhysRevD.87.112005`.

[36] Torben Ferber et al. *Displaced or invisible? ALPs from B decays at Belle II*. 2022. arXiv: `2201.06580 [hep-ex]`.

[37] N. Gubernari, A. Kokulu, and D. van Dyk. "$B \to P$ and $B \to V$ form factors from B-meson light-cone sum rules beyond leading twist". In: *Journal of High Energy Physics* 2019.1 (Jan. 2019). ISSN: 1029-8479. DOI: `10.1007/jhep01(2019)150`. URL: `http://dx.doi.org/10.1007/JHEP01(2019)150`.

[38] Sonia Carra et al. *Constraining off-shell production of axion-like particles with* $Z\gamma$ *and* WW *differential cross-section measurements*. 2021. arXiv: `2106.10085 [hep-ex]`.

Erklärung:

Ich versichere, dass ich diese Arbeit selbstständig verfasst habe und keine anderen als die angegebenen Quellen und Hilfsmittel benutzt habe.

Heidelberg, den 24. Januar 2022 ....Lara Grabitz........